ARL-TR-9072 ● SEP 2020

DEVCOM ARMY RESEARCH LABORATORY

Preliminary Investigation of Assimilating Global Synthetic Weather Radar

by Brian P Reen, Huaqing Cai, and John W Raby

NOTICES

Disclaimers

The findings in this report are not to be construed as an official Department of the Army position unless so designated by other authorized documents.

Citation of manufacturer's or trade names does not constitute an official endorsement or approval of the use thereof.

Destroy this report when it is no longer needed. Do not return it to the originator.

ARL-TR-9072 ● SEP 2020

Preliminary Investigation of Assimilating Global Synthetic Weather Radar

Brian P Reen, Huaqing Cai, and John W Raby
Computational Information Sciences Directorate, CCDC Army Research Laboratory

REPORT DOCUMENTATION PAGE

Form Approved
OMB No. 0704-0188

1. REPORT DATE *(DD-MM-YYYY)*	2. REPORT TYPE	3. DATES COVERED (From - To)
September 2020	Technical Report	January 2020–August 2020

4. TITLE AND SUBTITLE
Preliminary Investigation of Assimilating Global Synthetic Weather Radar

5a. CONTRACT NUMBER

5b. GRANT NUMBER

5c. PROGRAM ELEMENT NUMBER

6. AUTHOR(S)
Brian P Reen, Huaqing Cai, and John W Raby

5d. PROJECT NUMBER

5e. TASK NUMBER

5f. WORK UNIT NUMBER

7. PERFORMING ORGANIZATION NAME(S) AND ADDRESS(ES)
CCDC Army Research Laboratory
ATTN: FCDD-RLC-EM
2800 Powder Mill Road
Adelphi, MD 20783-1138

8. PERFORMING ORGANIZATION REPORT NUMBER
ARL-TR-9072

9. SPONSORING/MONITORING AGENCY NAME(S) AND ADDRESS(ES)

10. SPONSOR/MONITOR'S ACRONYM(S)

11. SPONSOR/MONITOR'S REPORT NUMBER(S)

12. DISTRIBUTION/AVAILABILITY STATEMENT
Approved for public release; distribution is unlimited.

13. SUPPLEMENTARY NOTES
ORCID IDs: Brian Reen, 0000-0002-2031-4731; Huaqing Cai, 0000-0003-3918-4153

14. ABSTRACT
Global Synthetic Weather Radar (GSWR) is a promising dataset to assimilate for improving short-term weather forecasts because it provides near-global coverage of certain fields normally obtained via radar. This report documents what appears to be the first attempt to assimilate GSWR data in a numerical weather prediction model. Derived from sources including satellite-based instrumentation, the GSWR column maximum reflectivity is used to create an estimated vertical profile of reflectivity, which is then converted to a heating term and assimilated using methods demonstrated in previous work with radar data. The assimilation technique is modified to better assimilate the GSWR data; these modifications include allowing the GSWR data to directly modify precipitation hydrometeors, cloud water, and water vapor. The assimilation of the GSWR data shows improvement in short-term forecasts of the placement of moist convection for the two cases studied. Further work is needed to expand to additional cases, continue to improve the assimilation method, and evaluate GSWR data and model forecasts assimilating GSWR against radar observations.

15. SUBJECT TERMS
mesoscale model, assimilation, numerical weather prediction, radar, satellite, WRF, verification

16. SECURITY CLASSIFICATION OF:			17. LIMITATION OF ABSTRACT	18. NUMBER OF PAGES	19a. NAME OF RESPONSIBLE PERSON
a. REPORT	b. ABSTRACT	c. THIS PAGE			Brian Reen
Unclassified	Unclassified	Unclassified	UU	49	19b. TELEPHONE NUMBER (Include area code) 301-394-3072

Contents

List of Figures

List of Tables

Acknowledgments

The US Army Combat Capabilities Development Command Aviation and Missile Center provided funding that helped support the research described in this technical report. Haig Iskenderian (Massachusetts Institute of Technology – Lincoln Laboratory) provided sample Global Synthetic Weather Radar data for use in this investigation.

The Model Evaluation Tools (MET) was used for verification. MET was developed by the National Center for Atmospheric Research (NCAR) through grants from the US Air Force Weather Agency and National Oceanic and Atmospheric Administration. The NCAR Command Language was used for creating some of the graphics in this report (http://dx.doi.org/10.5065/D6WD3XH5).

1. Introduction

Weather radar provides a potentially valuable data source for assimilation into numerical weather prediction (NWP) models due to its high temporal and spatial resolution; however, it is only available for limited portions of the earth. This value has led to its use in operational US National Weather Service hourly updating models including the 13-km Rapid Refresh (Benjamin et al. 2016) and the 3-km High-Resolution Rapid Refresh (HRRR; Alexander et al. 2017). In previous work (Reen et al. 2019), we used the Advanced Research version of the Weather Research and Forecasting model V3 (WRF-ARW; Skamarock et al. 2008) to adapt the assimilation method used by HRRR over the continental United States (CONUS) to a non-CONUS location with an isolated weather radar and demonstrated that assimilation of the radar data could still provide notable improvement in short-term forecasts of moist convection. The application described in Reen et al. (2019) differed from HRRR in that it relied on a single weather radar rather than a network of radars, used a much smaller domain, and did not have output from previous cycles of a radar-assimilating model to provide radar-enhanced initial conditions.

Although weather radar data are valuable for improving short-term forecasts of moist convection, it is only available over portions of the earth, and thus alternate data sources are desirable to improve forecasts over the vast areas where radar data are not available. While data sources such as radiosondes, surface observations, and aircraft observations are valuable for improving NWP forecasts, none of these provide spatial or temporal resolution anywhere near that provided by radar data. Satellite data sources are promising given the spatial coverage available from satellites. However, to provide near-global coverage, one would need to rely on a variety of satellites, each with its own data characteristics, and determine how to convert that to a field that can be assimilated to improve short-term forecasts of moist convection.

The Air Force is in the process of operationalizing a data product that uses machine learning to create a model that converts satellite data into radar-like fields. This product is called Global Synthetic Weather Radar (GSWR; Veillette et al. 2020) and a preliminary test of its assimilation is described in this study. The GSWR provides much broader coverage than radar data and since the fields that it provides are fields normally produced by radar, radar assimilation methods can be modified to ingest GSWR data.

Section 2 briefly describes GSWR data, Section 3 overviews the NWP model and its configuration, Section 4 gives a case description, and Section 5 discusses the assimilation methodology. Section 6 provides an overview of the experiment design, Section 7 describes the results, and a summary and a discussion of future work are provided in Section 8.

2. Global Synthetic Weather Radar

GSWR is being developed by Massachusetts Institute of Technology – Lincoln Laboratory as a near-global extension of the Offshore Precipitation Capability (Veillette et al. 2018) they developed for the Federal Aviation Administration for areas near CONUS (Veillette et al. 2020). GSWR uses machine learning to allow radar fields to be estimated where radar data are not available. One input for the convolutional neural network is satellite data, which includes the US Geostationary Operational Environment Satellite (GOES) satellites GOES-16 and GOES-17, the European satellites Meteosat-8 and Meteosat-11, and the Japanese satellite Himawari-8. Other input data are lightning data via the Vaisala Global Lightning Dataset 360, and numerical weather prediction output from the Air Force Global Air-Land Weather Exploitation Model. The truth used in creation of their model is space-based radar (National Aeronautics and Space Administration's Global Precipitation Measurement satellite's Dual-frequency Precipitation Radar). GSWR produces estimates of vertically integrated liquid, echo tops, and column maximum reflectivity (CMR). CMR is the GSWR output field used in this study.

GSWR data are to be available every 15 min, although in the test data, they were provided four times per hour, the time between output varied within the hour (being available at 13, 23, 43, and 53 after each hour). GSWR data cover at least 67 S to 67 N at all longitudes but the latitude it extends to varies between 67 and 70 depending on longitude. GSWR is available at 5-km horizontal grid spacing.

3. Model Description and Configuration

WRF-ARW (often simply called WRF) v4.1.2 (Skamarock et al. 2019) is used in this study. Preparation of initial conditions and boundary conditions was facilitated via the Weather Running Estimate–Nowcast Realtime system (WREN_RT; Reen and Dawson 2018). While WREN_RT can also run WRF, it cannot currently process GSWR data, so WREN_RT could not provide an end-to-end solution for this case. Plans are in place to extend WREN_RT to process GSWR data.

WRF was configured with 9-, 3-, and 1-km nested domains over two locations. The domains have 151 × 151, 151 × 151, and 199 × 199 horizontal grid points for the three domains and 56 vertical levels. One case has its WRF domains centered over the Black Sea (43.25 N, 29.83 E; Fig. 1) and the other over far western Russia, southwest of Moscow (54.00 N, 34.33 E; Fig. 2). The first guess for initial conditions is supplied by 0.25° resolution (Black Sea case) or 0.50° resolution (far western Russia case) Global Forecast System (GFS) data.

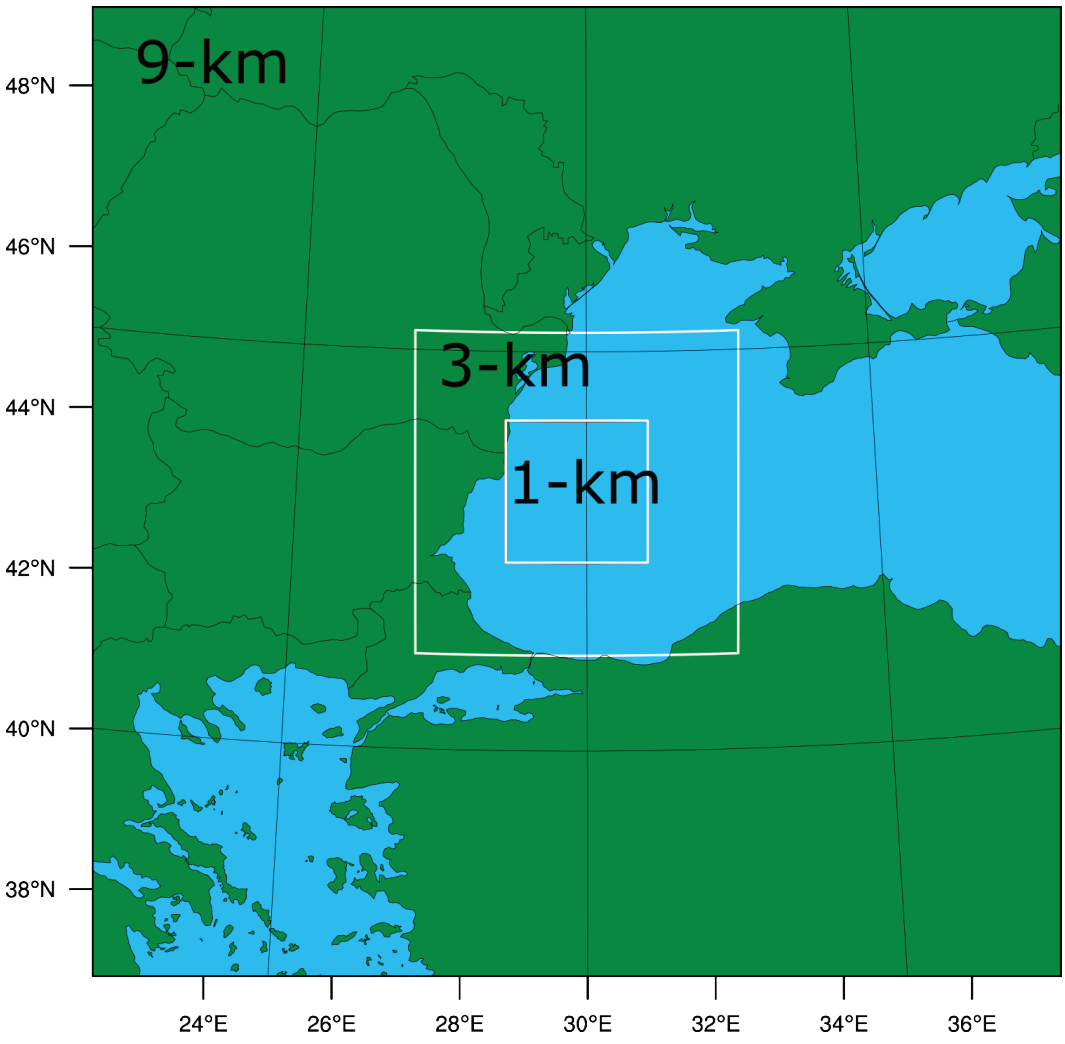

Fig. 1 Location of domains for Black Sea case

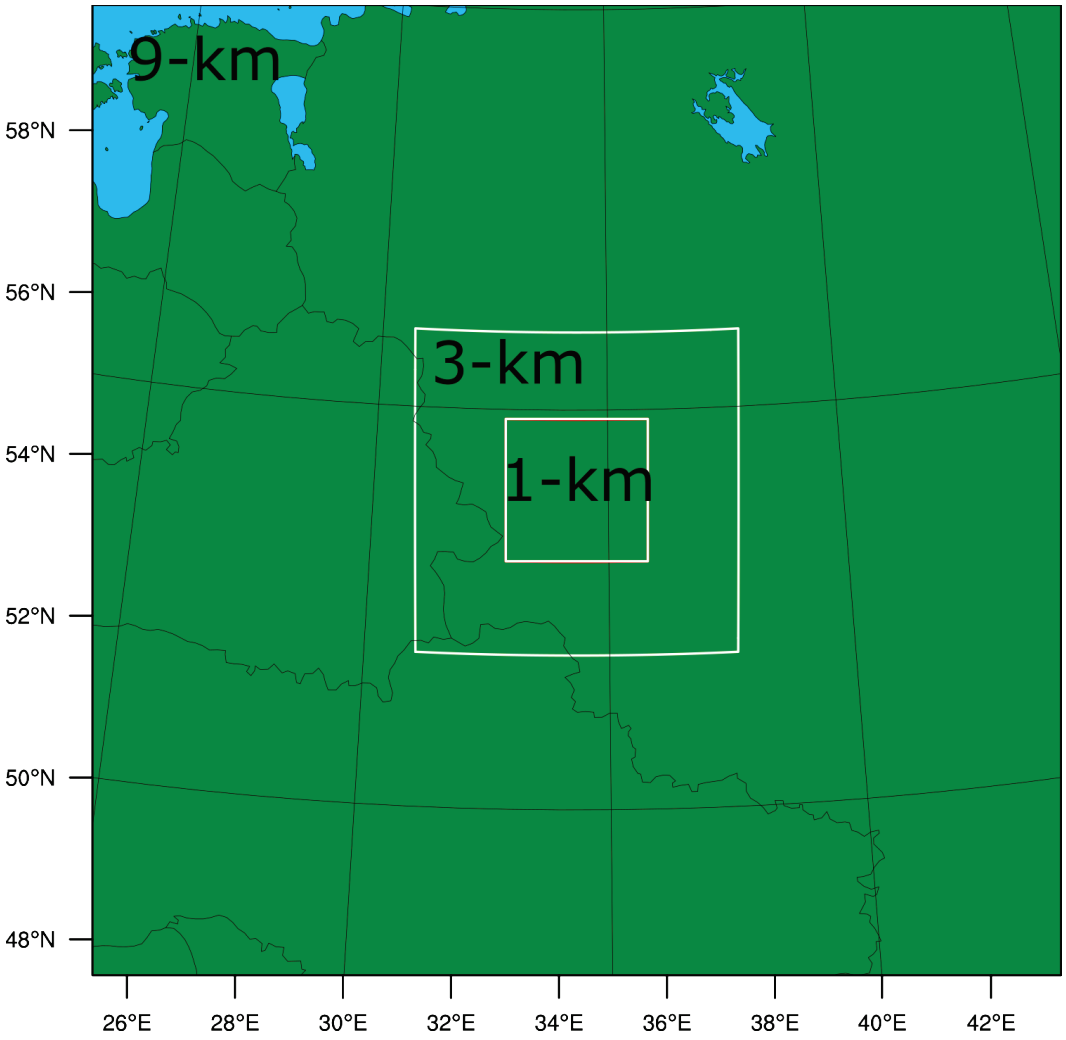

Fig. 2 Location of WRF domains for far western Russia case

WRF requires the user to choose parameterizations to represent various processes. The planetary boundary layer scheme used here was the level 2.5 Mellor–Yamada Nakanishi Niino scheme (MYNN; Nakanishi and Niino 2006; Nakanisho and Niino 2009; Olsen et al. 2019). For microphysics the aerosol-aware Thompson microphysics scheme (Thompson and Eidhammer 2014) was used. The Noah land surface model (Tewari et al. 2004) was used, and for radiation, the RRTMG (rapid radiative transfer model for general circulation models) shortwave and longwave radiation schemes (Iacono et al. 2008) were used. The Grell–Freitas cumulus parameterization scheme (Grell and Freitas 2014) is used on all domains. Although cumulus parameterization schemes are generally meant only for application on coarser domains where processes are not sufficiently represented, the Grell–Freitas scheme is intended to be scale-aware and adjust its impact based on the grid spacing of the model domain. Thus, in theory it should be able to be used for domains with any horizontal grid spacing. The parameterizations used in this study differ from

Reen et al. (2019) because the area simulated in that study was over the tropics, whereas this study is not.

4. Case Description

Two cases were examined in this study, one centered over the Black Sea (Fig. 1) and the other centered over far western Russia (Fig. 2). Both cases occurred on 15 July 2019; the Black Sea case covered 0300–1500 coordinated universal time (UTC), while the far western Russia case covered 0700–1900 UTC.

While the GSWR CMR ($GSWR_{CMR}$) is available four times an hour, for brevity the hourly values for the Black Sea case over the WRF 1-km domain are shown in Fig. 3. A large area of convection is seen in the eastern half of the domain from about 0300 to 0600 UTC. However starting around 0700 UTC, a single area of stronger reflectivity is the dominant feature; this continues until the end of the period at 1400 UTC.

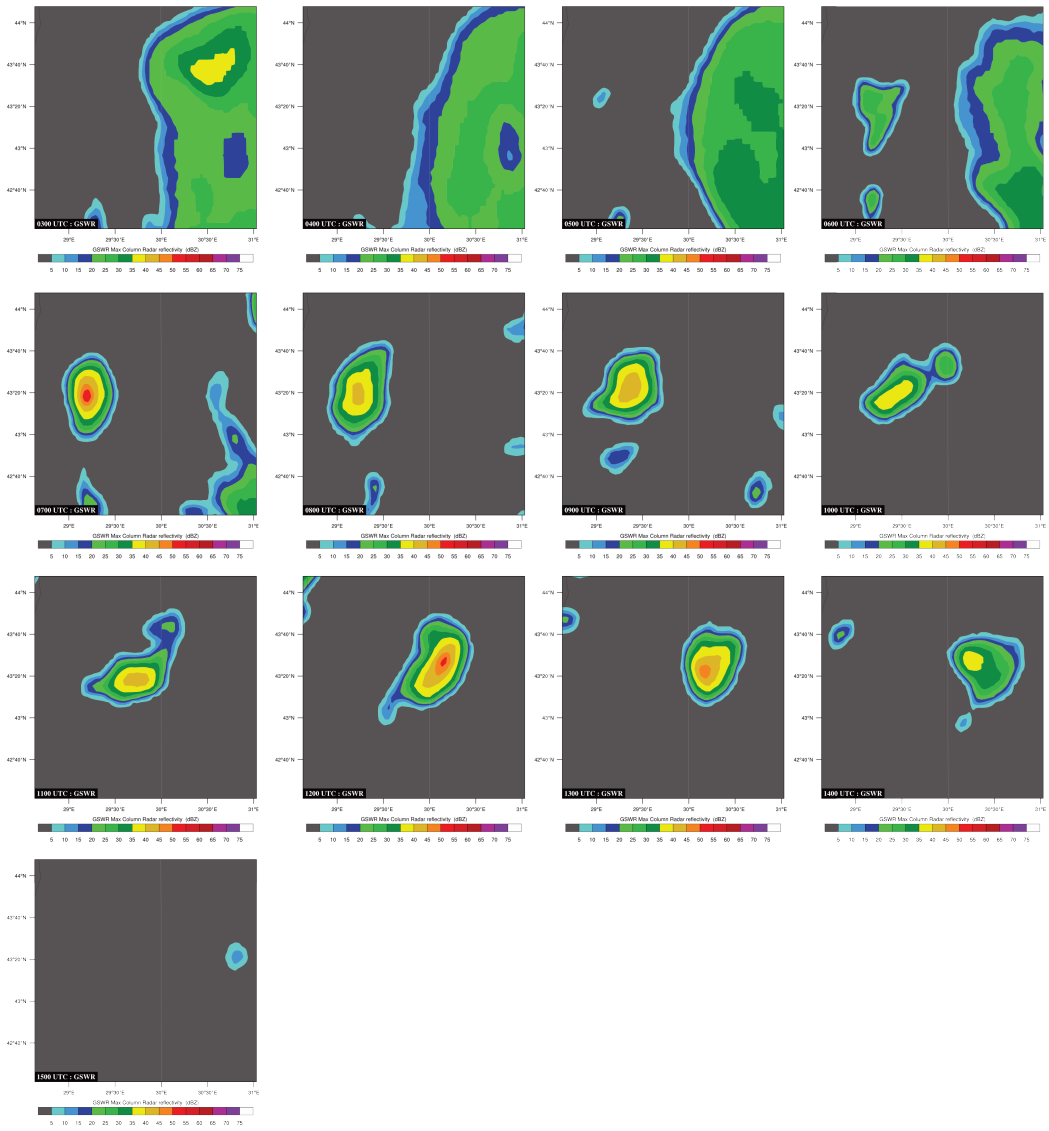

Fig. 3 Hourly GSWR$_{CMR}$ over the 1-km Black Sea domain for the entire length of the model integration. Note that 0900 UTC is the 0-h forecast time.

The hourly plots of GSWR$_{CMR}$ for the 1-km domain in the far western Russia case are shown in Fig. 4. An area of reflectivity is seen in the first hour, but then GSWR$_{CMR}$ shows little activity until an area of reflectivity begins moving into the southwest corner around 1200 UTC. This area appears to continue advecting through the domain for the next couple hours, while at the same time an area of reflectivity develops in the northern portion of the domain. An area of reflectivity starts moving into the northwestern part of the domain around 1400 UTC. The convection continues to evolve, and by 1800 UTC, there is almost no reflectivity in the domain.

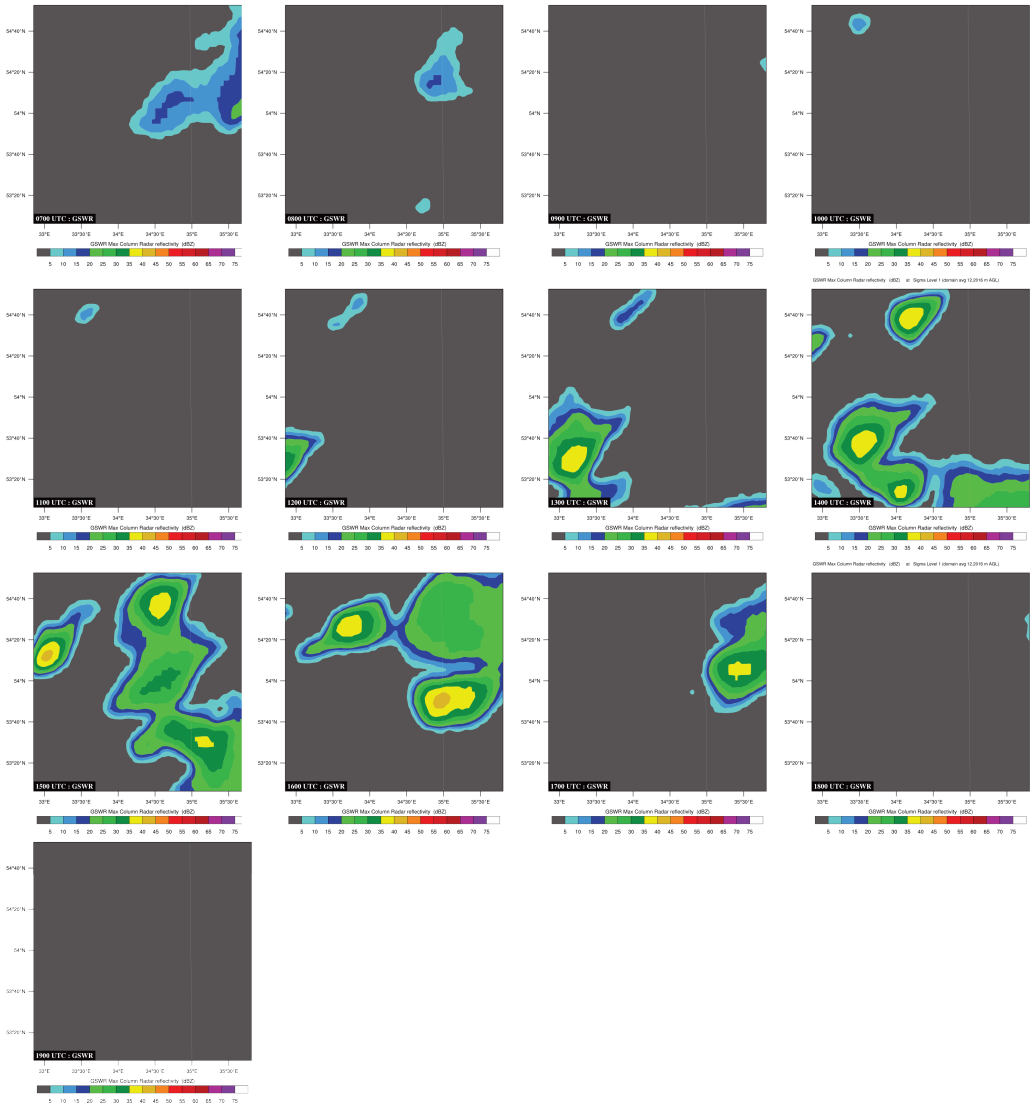

Fig. 4 Hourly GSWR$_{CMR}$ over the 1-km far western Russia domain for the entire length of the model integration. Note that 1300 UTC is the 0-h forecast time.

5. Assimilation Methodology

This section first discusses the methodology used to convert the 1-D GSWR$_{CMR}$ into 3-D GSWR$_{ref}$. Then the methodology used to convert GSWR$_{ref}$ to a latent heating term is described. Finally, the methods used to apply the latent heating term to the NWP model are described.

5.1 Determine 3-D Reflectivity

The goal in this work is to adapt the assimilation methodology used to assimilate radar reflectivity in Reen et al. (2019) to the GSWR data. The radar assimilation methodology of Reen et al. (2019) cannot be directly used for GSWR data because the radar assimilation involved 3-D radar reflectivity, whereas the GSWR data do not provide 3-D radar reflectivity but rather the maximum reflectivity in each column (i.e., CMR).

Thus, to assimilate GSWR data one must somehow create a profile of reflectivity based on the CMR. Reen et al. (2019) used the data assimilation package Gridpoint Statistical Interpolation (GSI; Shao et al. 2016) to convert radar reflectivity into latent heating terms for application in WRF. The GSI code uses a set of reference reflectivity profiles to vertically extend the reflectivity profiles beyond what is observed by the radar. We leverage these profiles from GSI V3.6 to provide a first guess of a vertical reflectivity profile based on the $GSWR_{CMR}$. The profiles provided in GSI reach from 0.2 to 16.0 km above ground level and are specified as values from 0 to 1 that are multiplied by CMR to provide a reflectivity profile. Different profiles are provided for each 5-dBZ range from 20 to 50 dBZ. While the GSI source code includes different profiles for summer and winter, GSI V3.6 is hardcoded to only use the summer profiles and those are the profiles we use in this study. For $GSWR_{CMR}$ less than 20 dBZ, we used the profiles GSI used for 20 dBZ, and for $GSWR_{CMR}$ greater than 50 dBZ, we used the profiles GSI used for 50 dBZ. Since GSI specifies the profiles as values between 0 and 1 that are multiplied by $GSWR_{CMR}$, using profiles outside of their ranges will still result in the generated profile having the desired CMR. Examples of the reflectivity profiles that result from a $GSWR_{CMR}$ of 35 and 44 dBZ are shown in Fig. 5.

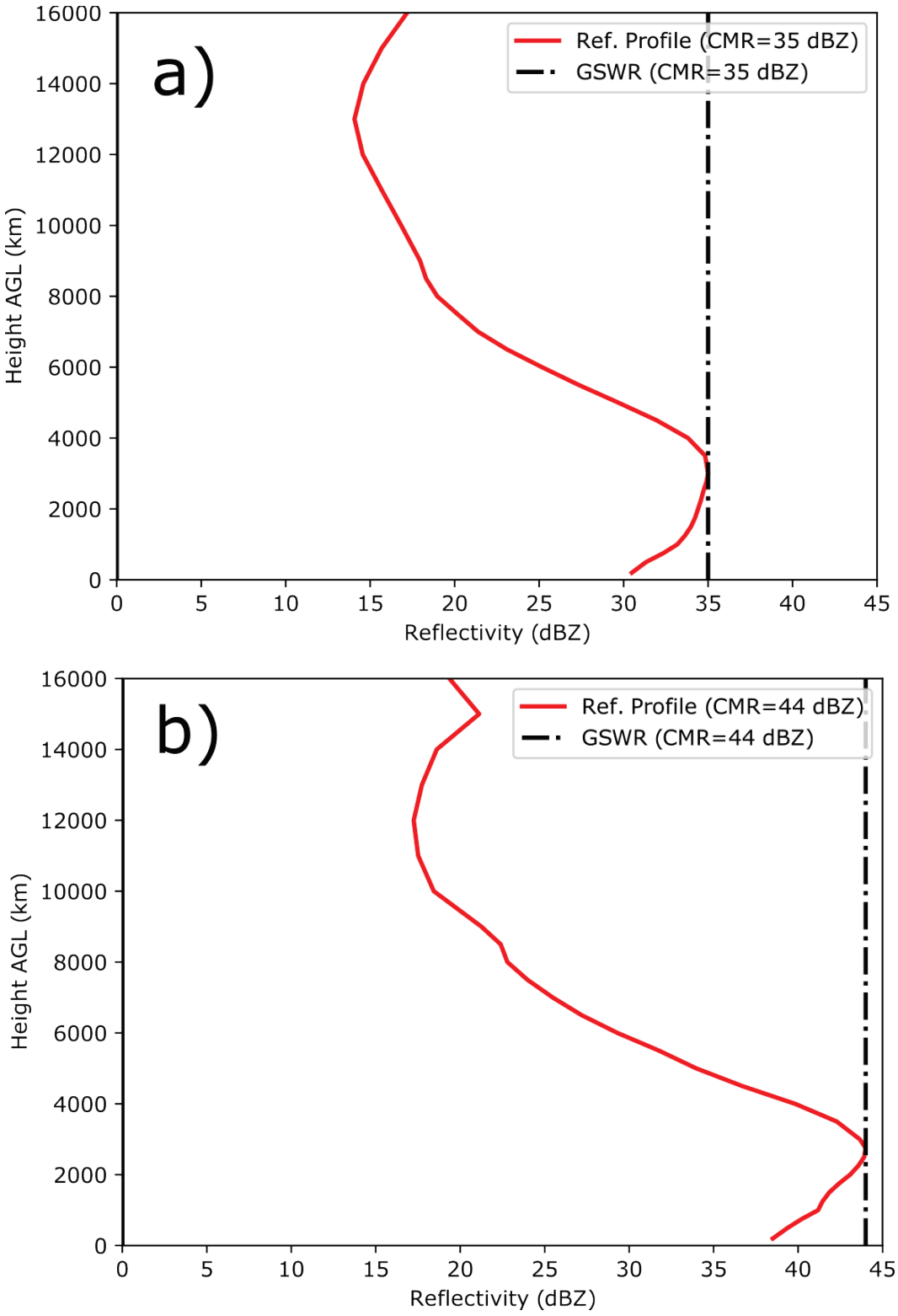

Fig. 5 Reference profiles generated based on GSI profiles for a CMR of a) 35 dBZ and b) 44 dBZ

While the GSI profiles provide a first guess of a reflectivity profile appropriate for a given $GSWR_{CMR}$, it would be better to utilize more case-specific information. One method to do this is to leverage the WRF reflectivity profile to convert the $GSWR_{CMR}$ into a reflectivity profile. This is accomplished by scaling the WRF reflectivity (WRF_{ref}) by a factor so that its adjusted CMR is equal to the $GSWR_{CMR}$. Thus, we calculate a GSWR-derived reflectivity profile ($GSWR_{ref}$) as follows: $GSWR_{ref} = WRF_{ref} * (GSWR_{CMR}/WRF_{CMR})$. This method allows the case-specific WRF reflectivity profile to be leveraged in assimilating GSWR. This obviously cannot be used for columns where WRF does not forecast moist convection and so the GSI profiles are retained for cases where the WRF_{CMR} is too weak. Specifically, we require the WRF_{CMR} to be at least half the $GSWR_{CMR}$ (i.e., $WRF_{CMR} \geq 0.5 * GSWR_{CMR}$). Thus, even when WRF_{CMR} greater than 0, we do not necessarily use WRF_{ref} in creating $GSWR_{ref}$; this is because it is anticipated that scaling too-weak profiles will result in an unrealistic profile. This threshold ratio (0.5) for using WRF reflectivity profiles should be considered preliminary and may need to be adjusted based on future research.

Figures 6 and 7 illustrate this technique. In Fig. 6a, at a hypothetical WRF grid point $GSWR_{CMR}$ is 34 dBZ and WRF_{ref} is as shown with WRF_{CMR} equal to 15 dBZ. Since [WRF_{CMR} = 15 dBZ] < [0.5 * ($GSWR_{CMR}$ = 34 dBZ) = 17 dBZ], WRF_{ref} is considered too weak to scale to create $GSWR_{ref}$. Thus, the $GSWR_{ref}$ calculated for this point and shown in Fig. 6b is defined using the reference GSI profiles. In contrast to this, at the hypothetical WRF grid point in Fig. 7a, $GSWR_{CMR}$ is also 34 dBZ, but the WRF_{ref} has WRF_{CMR} equal to 20 dBZ. Since [WRF_{CMR} = 20 dBZ] > [0.5 * ($GSWR_{CMR}$ = 34 dBZ) = 17 dBZ], WRF_{ref} is considered strong enough to scale to create $GSWR_{ref}$. Therefore, the $GSWR_{ref}$ calculated for this point and shown in Fig. 7b is defined by scaling WRF_{ref}.

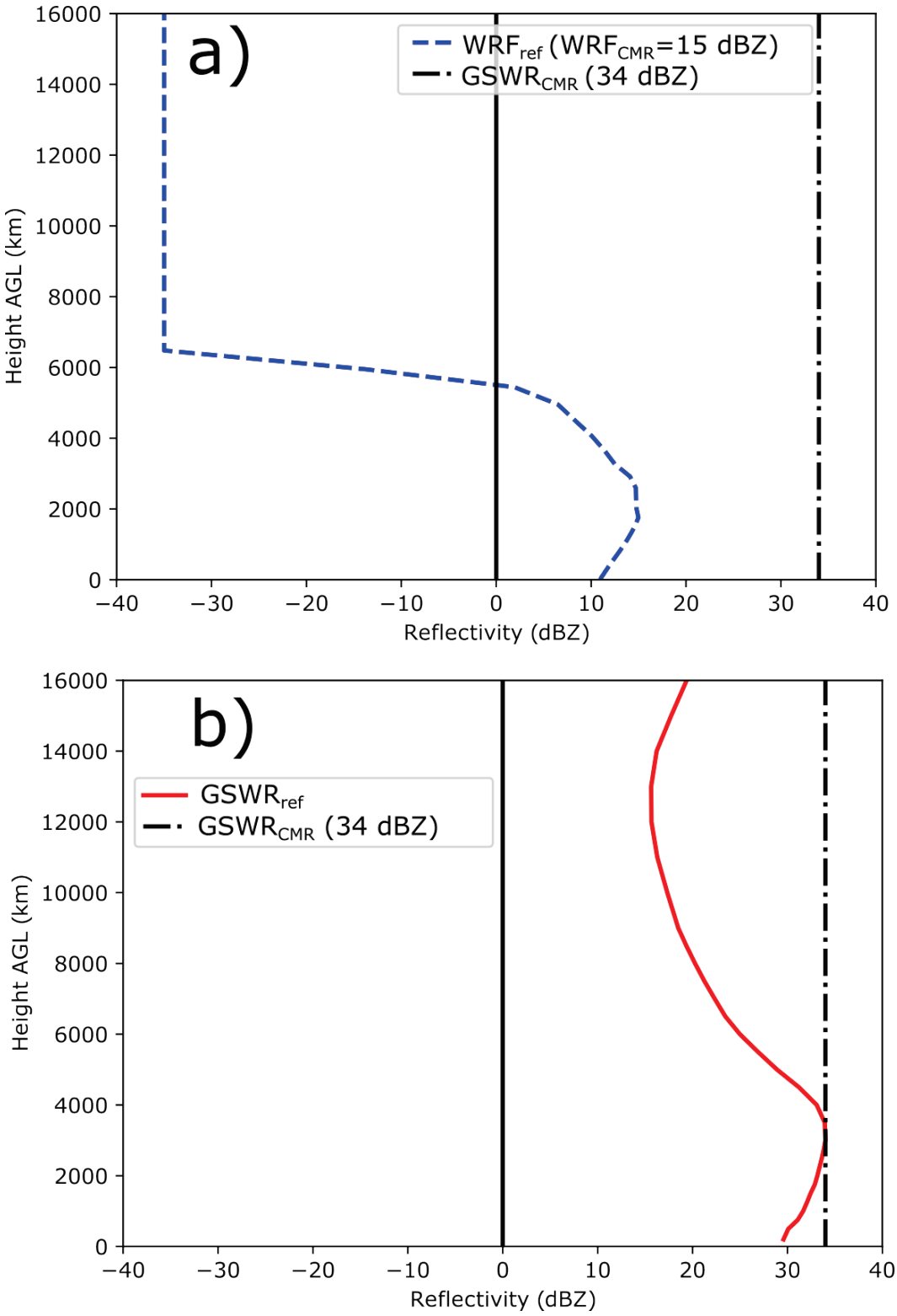

Fig. 6 Hypothetical GSWR$_{CMR}$ plotted with a) coincident WRF$_{ref}$ and b) the resulting GSWR$_{ref}$ calculated from GSI reference profiles

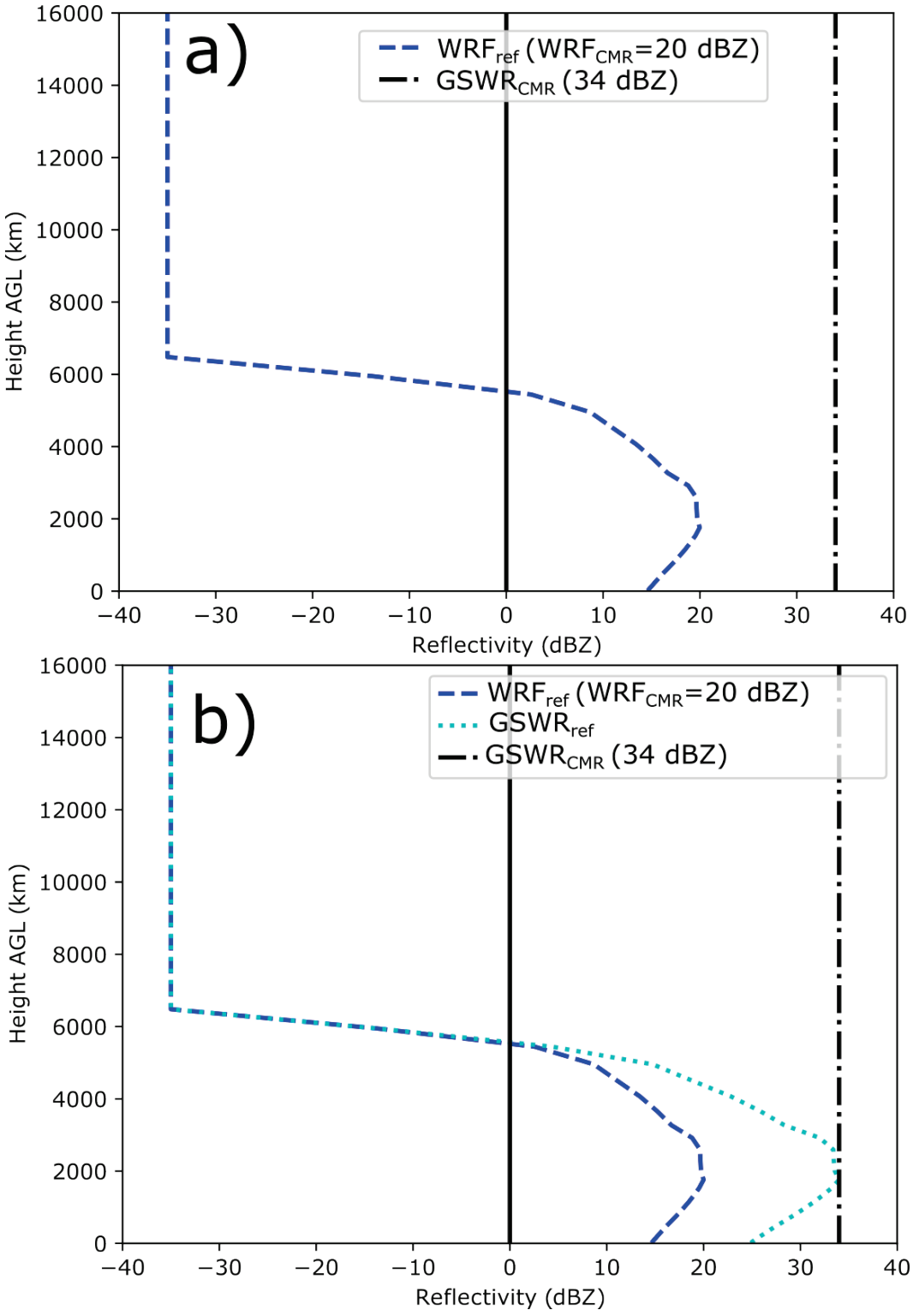

Fig. 7 Hypothetical GSWR$_{CMR}$ plotted with a) coincident WRF$_{ref}$ and b) the resulting GSWR$_{ref}$ calculated by scaling WRF$_{ref}$ by GSWR$_{CMR}$/WRF$_{CMR}$

5.2 Determine Latent Heating

Once $GSWR_{ref}$ is calculated, the reflectivity is used to calculate the reflectivity-derived latent heating (RDLH) using the same equations applied to 3-D radar reflectivity in Reen et al. (2019) via use of GSI. However, note that Reen et al. (2019) incorrectly reported RDLH was a temperature tendency when in reality it is a potential temperature tendency. To determine RDLH, first use the reflectivity factor to approximate the rain/snow condensate (*f[Z_e]*) it represents using the equation from GSI:

$$f[Z_e] = \frac{1.5}{264083} * 10^{(Z/17.8)}, \quad (1)$$

where

Z = radar reflectivity

Then the RDLH is calculated using the following equation:

$$\text{RDLH} = \left(\frac{d\theta}{dt}\right)_{LH} = \left(\frac{1000}{p}\right)^{R_d/c_p} * \frac{(L_v+L_f)(f[Z_e])}{t_c c_p}, \quad (2)$$

where

p = pressure (hPa)

R_d = dry gas constant (≈287.059)

c_p = specific heat of dry air at constant p (≈1004.705 J kg^{-1} K^{-1}) — R_d/c_p is 1/3.5

L_v = latent heat of vaporization at 0° C (2.501E6 J kg^{-1})

L_f = latent heat of fusion at 0° C (0.3335E6 J kg^{-1})

t_c = time period of condensate formation (in seconds, here set to 15*60)

θ = potential temperature

t = time

LH = latent heating

f[Z_e] = reflectivity factor converted to rain/snow condensate

RDLH is set to zero if echoes are weak. Namely, if $GSWR_{ref}$ does not equal or exceed 5 dBZ, then RDLH is set to zero. This is more restrictive than the 0.001-dBZ criteria used for radar in Reen et al. (2019) as experimentation indicated that GSWR sometimes showed widespread weak dBZ values that it was suspected were not consistent with reality. Also, RDLH is set to zero throughout a column if after horizontal smoothing of RDLH (yielding $RDLH_{smooth}$), no vertical layer in a column

of RDLH exceeds 0.00002 Ks^{-1}. Since GSWR data were processed via a Python script rather than via GSI a different smoothing was used here than with the radar data. Specifically, gaussian_filter from scipy.ndimage (https://docs.scipy.org/doc/scipy/reference/generated/scipy.ndimage.gaussian_filter.html#scipy.ndimage.gaussian_filter) was used with x and y sigma both set to 0.7.

Unlike the radar data in Reen et al. (2019), RDLH is not set to zero where temperature is greater than 277.15 K and reflectivity is less than 28 dBZ. It is not known why these criteria were used in GSI to prevent relatively weaker reflectivities from being used to create RDLH when the temperature was at least 4 °C above freezing. Also, unlike the radar processing, RDLH is not set to zero within the atmospheric boundary layer. Since we do not know the atmospheric boundary layer depth while processing GSWR data, we instead modify WRF to create an option as to whether RDLH should be excluded from the atmospheric boundary layer. That option was not enabled for the experiments in this study and so GSWR-derived RDLH were applied within the planetary boundary level.

In the top level of the field where RDLH is stored, a flag is stored indicating whether convection should be suppressed in cumulus parameterizations. This flag is set based on $RDLH_{smooth}$ to indicate a) insufficient information is available to set the flag (–10; i.e., missing), b) no convection in the column (0), or c) there may be convection in the column (1).

5.3 Apply Latent Heating

Once RDLH is calculated, one must determine how to apply it in WRF. The basic methodology is shown in Fig. 8 and generally follows that used by Reen et al. (2019). The goal is to induce or suppress moist convection in WRF so that WRF forecast coverage of moist convection will be consistent with GSWR. The primary method by which RDLH influences the model is through its replacement of the microphysics heating term (MPHT) and the cumulus parameterization heating term (CPHT). The WRF microphysics parameterization calculates MPHT and the WRF cumulus parameterization scheme calculates CPHT, and if RDLH were not being applied, the MPHT and CPHT would be applied to the model. Similarly, if RDLH is missing for a particular grid cell (e.g., if the domain reaches into the arctic and beyond the range of GSWR), the MPHT and CPHT is applied (case 1 in Fig. 8). If the RDLH is zero (case 2 in Fig. 8), instead of applying the MPHT the zero heating term calculated by RDLH is applied and this serves to suppress moist convection; however, in this case the CPHT is applied. If the RDLH is positive (case 3 in Fig. 8), then the method will apply the RDLH in place of the MPHT. If the magnitude of the RDLH is non-negligible ($\geq 1.0 * 10^{-7}$ Ks^{-1}), then CPHT will not be applied. The

setting of CPHT to zero when RDLH has a non-negligible positive value was not relevant to Reen et al. (2019) because radar was only assimilated on the innermost domain, and that domain was not using a cumulus parameterization. Unlike the radar assimilation in Reen et al. (2019), there are some exceptions to the use of RDLH in place of MPHT when RDLH is greater than 0.

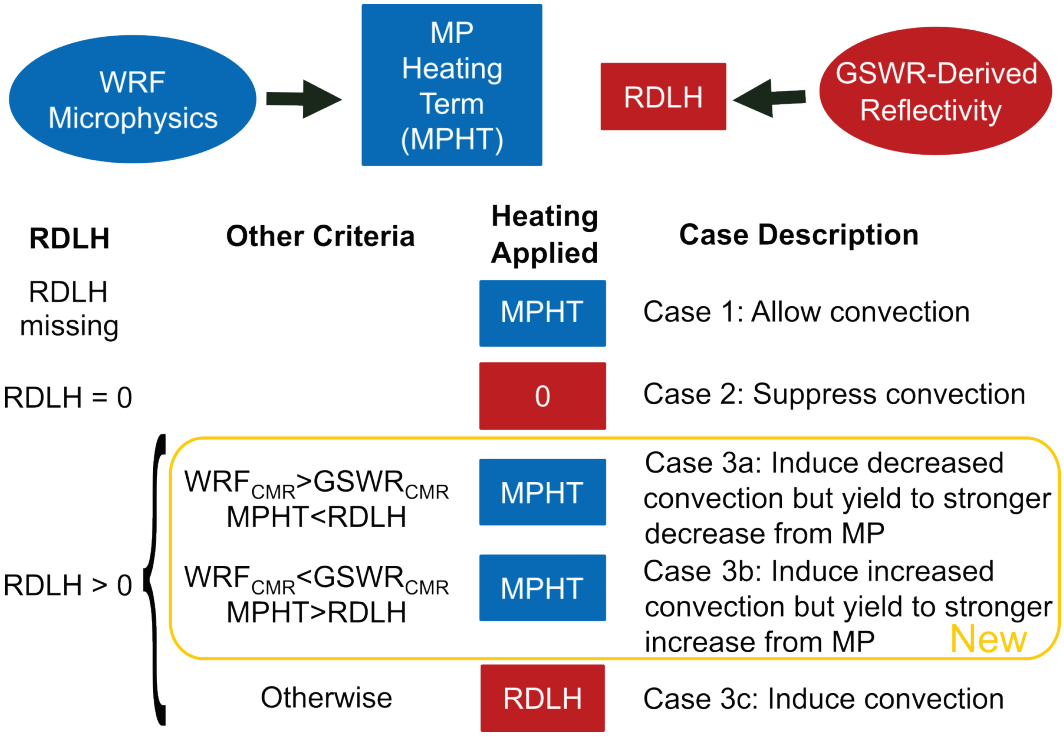

Fig. 8 Diagram illustrating whether MPHT or RDLH is applied based on RDLH, MPHT, WRF_{CMR}, and $GSWR_{CMR}$. The orange box indicates the portion of the algorithm that is new and used with GSWR assimilation compared to the technique used for radar observations in Reen et al. (2019).

The exceptions to the replacement of MPHT by RDLH if RDLH is greater than 0 are in place because the vertical structure of RDLH is an estimation. Unlike the radar assimilation where a vertical profile of reflectivity produced a vertical profile of RDLH, with GSWR the CMR is used with other information to estimate a vertical profile of reflectivity from which a vertical profile of RDLH is created. Therefore, with the GSWR assimilation, we have less confidence in the vertical structure of RDLH than we had with radar data. The exceptions allow the MPHT to be used if the MPHT would more strongly push the model in the direction the RDLH is attempting to push the model.

One of the exceptions is that if WRF_{CMR} is greater than $GSWR_{CMR}$ and MPHT is less than RDLH then we apply MPHT instead of applying RDLH (case 3a in Fig. 8). In this case WRF is showing stronger convection than GSWR indicates

should be present, and thus the goal is to weaken the convection by applying RDLH. However, if MPHT is less than RDLH, then applying MPHT will be even more effective in weakening convection than RDLH and so allowing MPHT to be applied does not hinder our goal of weakening moist convection. The other exception (case 3b in Fig. 8) is the mirror image of the first. Namely, if WRF_{CMR} is less than $GSWR_{CMR}$ and MPHT is greater than RDLH, then we again apply MPHT instead of applying RDLH. In this case WRF is showing weaker convection than GSWR indicates, and thus we want to strengthen the convection by applying RDLH. However, when MPHT is greater than RDLH applying MPHT will more quickly strengthen convection than RDLH and so applying MPHT is not counter to our goal of strengthening moist convection. Neither of these exceptions should ultimately overweaken nor overstrengthen moist convection, since they are dependent on the current relationship between WRF_{CMR} and $GSWR_{CMR}$.

These exceptions are important as they allow the vertical structure to more easily evolve in a manner consistent with the environment. Without the exceptions in place, in cases where the WRF_{CMR} is large enough that WRF_{ref} is scaled to create $GSWR_{ref}$, the evolution of the vertical reflectivity profile may be overly constrained. When we scale WRF_{ref} to create $GSWR_{ref}$, we are assuming that the shape of the vertical WRF reflectivity profile is correct, but that its magnitude is incorrect; thus, we assume that to get the true reflectivity profile we just need to scale the WRF reflectivity profile. However, our source of "truth" is the GSWR data, which does not tell us the shape of the vertical profile. While the shape of the profile we are imposing is our best guess, due to the shape not being prescribed by observations we should not too strongly impose the shape. By replacing the heating term that the model microphysics scheme produces (MPHT) with the RDLH based on the current shape of the WRF reflectivity profile we reinforce the current shape of the WRF reflectivity profile and suppress the ability of the microphysics scheme to modify the vertical shape of the reflectivity profile. The previously described exceptions to the methodology provide an opportunity for WRF to evolve the vertical shape of the reflectivity profile while still mandating that the solution is being pushed sufficiently strongly toward stronger or weaker moist convection (as determined by the relationship between $GSWR_{CMR}$ and WRF_{CMR}).

The overall process of creating and applying RDLH described in this section is shown in Fig. 9. This flowchart indicates the parts of the process that were used with radar data in Reen et al. (2019) but are not used here ("Old"), parts that are used with GSWR data but not radar data ("New"), and parts that are used with both radar and GSWR data ("Same").

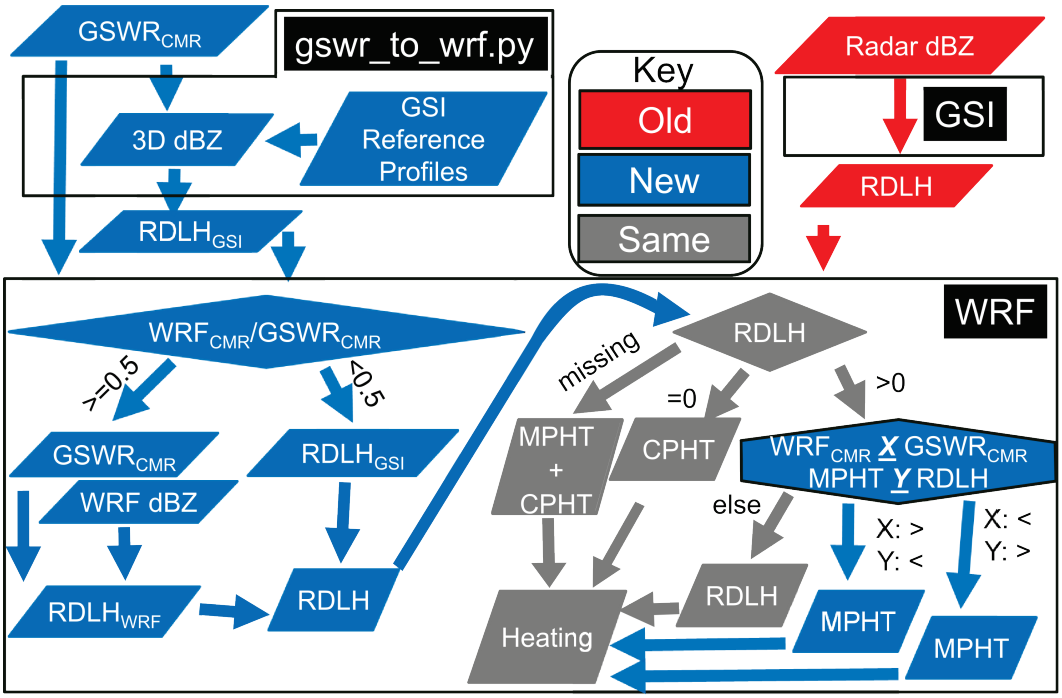

Fig. 9 Flowchart summarizing the similarities and differences between the processing of radar data and GSWR data. Parts of the flowchart relevant to processing radar but not GSWR data are labeled "Old"), parts of the flowchart relevant to processing GSWR but not radar data are labeled "New", and parts of the flowchart relevant to processing both radar and GSWR data are labeled "Same". Areas surrounded by thick black lines take place in the software program noted in white letters against a black background within the area outlined by the thick black lines.

Examining WRF output indicated that where $GSWR_{CMR}$ was large, the sudden imposition of a large RDLH could result in what appeared to be unrealistic waves spreading and have a negative impact on the solution. To mitigate this issue an equation to limit $GSWR_{ref}$ was added using the following adjustment of $GSWR_{ref}$:

$$GSWRref = MIN(MAX(WRFref + 10, 40), GSWRref) \quad (3)$$

The effect of this equation might be best seen through several examples as shown in Table 1. The equation prevents values of $GSWR_{ref}$ from being applied if they are greater than 40 dBZ and more than 10 dBZ greater than the reflectivity WRF currently predicts (WRF_{ref}). When there is a high $GSWR_{ref}$ value and the model shows reflectivity values noticeably weaker than this, the GSWR data will still be applied to strengthen moist convection at this point. As the moist convection in the model strengthens, WRF_{ref} will come closer to $GSWR_{ref}$ and one will be able to gradually increase the $GSWR_{ref}$ being applied to be closer to the actual $GSWR_{ref}$ value.

Table 1 Examples of the impact of the $GSWR_{ref}$ limiter equation

$GSWR_{ref}$ (original)	WRF_{ref}	$GSWR_{ref}$ (updated)
45	20	40
45	30	40
45	40	45
45	50	45
55	20	40
55	30	40
55	40	50
55	50	55

Note: All values dBZ

As noted in the previous section, horizontally smoothed RDLH is used to determine a flag for each column indicating whether convection is possibly present, not present, or alternatively that RDLH is missing. This flag is used in the Grell–Freitas cumulus parameterization used in this study to set a variable cap_max that appears to be the maximum pressure above ground at which a cloud base is allowed to be established (i.e., the maximum pressure difference between the ground and the cloud base). If convection is possibly present, then cap_max is set to 150 hPa; if convection is not present, then cap_max is set to 10 hPa; and if RDLH is missing, then cap_max is set to 75 hPa. The relative magnitude of the influence of RDLH on the model results via the cumulus parameterization versus via modification of the microphysics heating is not known. Given the relatively fine resolution of the innermost domain that is the focus of this study, it is anticipated that the scale-aware Grell–Frietas cumulus parameterization will have limited direct influence on the 1-km domain. In Reen et al. (2019), a different cumulus parameterization was used that was not scale-aware and thus it was not used on the finest domain, which is the only domain where RDLH was applied in that study. Additionally, the cumulus parameterization used in that study is not affected by RDLH.

If GSWR, via RDLH, indicates that there should be no moist convection at a location, then there should also not be any precipitation hydrometeors. While applying the RDLH of zero in this case should help suppress the formation of precipitation hydrometeors, directly modifying the prevalence of these hydrometeors may allow the WRF solution to more closely match GSWR. Therefore, an option was added to WRF that if the GSWR-derived reflectivity profile ($GSWR_{ref}$) results in a latent heating term of zero (RDLH = 0) but the model indicates nonzero precipitation hydrometeors, then actions are taken to decrease such hydrometeors. Specifically, at each time step the mixing ratio of rain, snow, graupel, and hail present is decreased by an amount that would result in them being completely removed in 1 h if there were no other tendency terms for these mixing ratios. Additionally, the cloud water mixing ratio is decreased each time step by an amount that would lead to it decreasing by 50% in 1 h. The modification of the

cloud water mixing ratio only takes place when RDLH = 0 and WRF has nonzero precipitation hydrometeors. Thus, while obviously cloud can be present when there is no reflectivity that would be seen by GSWR, the idea here is that if the model is erroneously creating precipitation hydrometeors, we can remove some of these precipitation hydrometeors by decreasing the amount of cloud water present.

Another option was added to directly decrease the water vapor mixing ratio in cases where RDLH = 0 and WRF has nonzero precipitation hydrometeors. The reasoning is that if the model is erroneously producing precipitation hydrometeors then it may be because the environment is too moist. For the water vapor mixing ratio, an amount is removed each time step that would result in the water vapor mixing ratio decreasing by 10% in 1 h (again, assuming there are no other terms affecting the water vapor mixing ratio).

The RDLH based on a given $GSWR_{CMR}$ field is applied over the 15 min leading up to the valid time of the $GSWR_{CMR}$ field (Fig. 10). Since the test $GSWR_{CMR}$ data were not at 15-min intervals, each 15-min time was assigned the nearest $GSWR_{CMR}$ data and the data were applied over the 15 min leading up to that time. While for clarity Fig. 10 illustrates a 1-h pre-forecast, for this study 6-h pre-forecasts were used based on the findings of Reen et al. (2019).

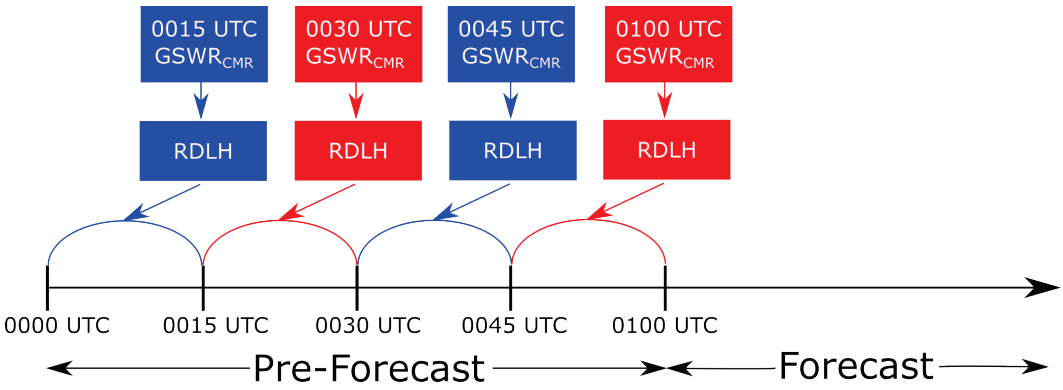

Fig. 10 Diagram illustrating the insertion of RDLH derived from 15-min $GSWR_{CMR}$ over the 15 min preceding the valid time of each $GSWR_{CMR}$ field over a 1-h pre-forecast in order to provide the best initial conditions for the forecast

6. Experimental Design

The experiments described in this report are shown in Table 2. Each experiment integrates a 6-h pre-forecast to spin up the simulation; for experiments employing data assimilation, the data assimilation is carried out during this period. The 6-h pre-forecast is followed by a 6-h forecast. The first experiment is Experiment (Exp.) Control and is the only experiment that does not assimilate the GSWR data. Exp. GSWR assimilates the GSWR data but without some of the enhancements of the

subsequent experiments. All experiments that assimilate GSWR data do so on all three domains. Exp. GSWR_H adds explicit adjustment of precipitation hydrometeors (including cloud water) based on RDLH. Exp. GSWR_HN adds observations to the initial condition analysis performed by the WRF-related program Obsgrid (NCAR 2019) and also performs observation nudging during the 6-h pre-forecast. The observations utilized are from the National Centers for Environmental Prediction Meteorological Assimilation Data Ingest System (MADIS; madis.noaa.gov). The MADIS observations used here include aircraft, maritime (i.e., from boats), Météorologique Aviation Régulière (METAR) surface observations, radiosondes, and satellite-derived wind. The non-GSWR observations are only assimilated in Exp. GSWR_HN. Exp. GSWR_HL adds to Exp. GSWR_H the reflectivity limiter that prevents $GSWR_{ref}$ values more than 10 dBZ greater than WRF_{ref} from being used when $GSWR_{ref}$ is greater than 40 dBZ. The final experiment, Exp. GSWR_HLV, enables the water vapor mixing ratio to be decreased based on $GSWR_{ref}$.

Table 2 Experimental design

Exp. Name	GSWR	Hydro-meteors	Obs in IC	Obs Nudging	Limiter	Water Vapor
Control	N	N	N	N	N	N
GSWR	Y	N	N	N	N	N
GSWR_H	Y	Y	N	N	N	N
GSWR_HN	Y	Y	Y	Y	N	N
GSWR_HL	Y	Y	N	N	Y	N
GSWR_HLV	Y	Y	N	N	Y	Y

Notes: N = No, Y = Yes, IC = Initial Conditions

All of these experiments are carried out for both the domains centered over the Black Sea and over far western Russia. The next section describes the results of these experiments.

7. Results

Verification for these two cases was performed by comparing WRF_{CMR} and $GSWR_{CMR}$. Although most of the experiments assimilated $GSWR_{CMR}$, the assimilation is carried out over the first 6 h of the simulation, whereas the verification is of the second and final 6 h of the simulation. Therefore, the verification is not against the same values that are being assimilated.

The Fractions Skill Score (FSS; Roberts 2008; Roberts and Lean 2008) and bias were used to evaluate the model forecasts. FSS is a neighborhood-based method

that compares every square neighborhood of a given size in the model domain with the coincident neighborhood in the observations (here GSWR) to see whether a reflectivity exceeding a given threshold occurs in one or both of the neighborhoods. In this study, an 11- × 11-km neighborhood size was used. The FSS of reflectivity forecasts provides information on how well the model places moist convection and does not penalize the model for errors below the scale of the neighborhood. The best possible FSS is 1.0. The bias score indicates how the fraction of the model domain exceeding a given reflectivity threshold (forecast rate) compares to the fraction of the coincident GSWR subset exceeding that same reflectivity threshold (observed rate) (i.e., bias = forecast rate/observed rate). The best possible bias score is 1.0. If the model has at least one grid cell that exceeds the reflectivity threshold and the observation has no grid cells that exceed the threshold, the FSS will necessarily be zero and bias will be undefined (due to division by zero). Similarly, if the model has no grid cells exceeding the reflectivity threshold and the observation has at least one grid exceeding the threshold, again FSS will be zero, but bias will be zero.

7.1 Black Sea Case

Figure 11 compares WRF_{CMR} for each of the experiments on the 1-km domain at the 0-h forecast time (0900 UTC) with the $GSWR_{CMR}$ valid at that time. The 0-h forecast time demonstrates the ability of the assimilation method to create a reflectivity consistent with $GSWR_{CMR}$. $GSWR_{CMR}$ indicates that the main feature at this time is an area with reflectivity reaching 40 dBZ in the central-to-northern portion of the western half of the domain (Fig. 11g). The experiment that does not assimilate GSWR data (Exp. Control, Fig. 11a) does not show this feature but does indicate a fairly large area with reflectivity along the eastern edge of the domain. The assimilation of GSWR data results in the reflectivity feature seen in the GSWR data being in the model solution (Exp. GSWR, Fig. 11b). Along the eastern edge of the domain, the apparently erroneous reflectivity has a lower maximum than seen without GSWR assimilation (and is somewhat westward compared to Exp. Control), but the model still overforecasts reflectivity in this area as evaluated against GSWR. Allowing GSWR to influence both precipitation hydrometeors and cloud water results in the observed feature remaining in the forecast but ameliorates the overforecast in the eastern part of the domain (Exp. GSWR_H, Fig. 11c). Adding the assimilation of other observations (both via an analysis at the start of model integration and via observation nudging) results (Exp. GSWR_HN, Fig. 11d) in little change from the previous experiment in terms of CMR, although the reflectivities in the southeast corner are decreased somewhat, which appears consistent with GSWR. Adding the limiter (to prevent shocks from large latent

heating terms suddenly being imposed) allows the main reflectivity feature seen in the GSWR data to remain in the WRF solution but noticeably increases the overforecast in the eastern two-thirds of the domain (Exp. GSWR_HL, Fig. 11e) compared to not using the limiter (Exp. GSWR_H, Fig. 11c). Finally, allowing GSWR to directly influence water vapor removes almost all of the overforecast and produces a CMR very similar to observations (Exp. GSWR_HLV, Fig. 11f).

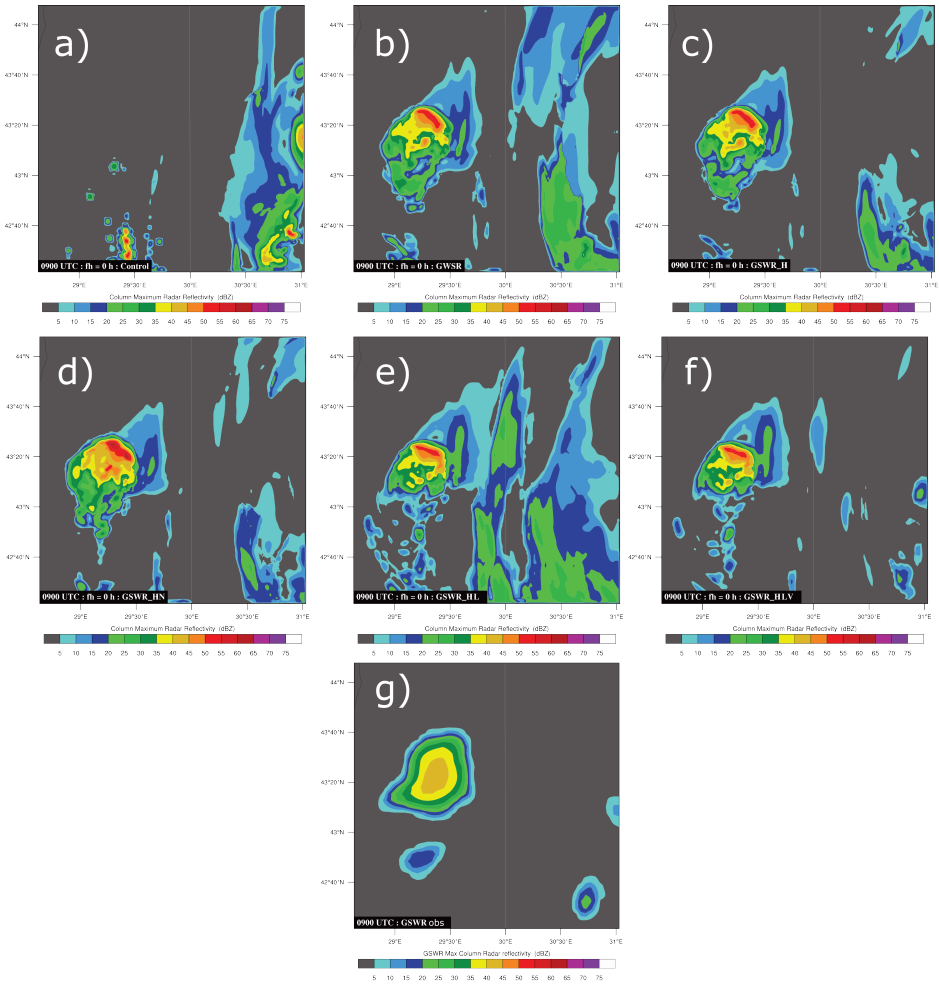

Fig. 11 WRF$_{CMR}$ for the Black Sea case for Exps. a) Control, b) GSWR, c), GSWR_H, d) GSWR_HN, e) GSWR_HL, f) GSWR_HLV at the 0-h forecast time (0900 UTC), and g) the GSWR$_{CMR}$ for 0900 UTC. In the lower-left-hand corner of the black box of each WRF$_{CMR}$ plot (a–f), the text "fh = 0 h" indicates that the 0-h forecast is plotted.

The verification statistics for the 1-km domain of the Black Sea simulations are shown in Fig. 12 (10 dBZ), Fig. 13 (20 dBZ), and Fig. 14 (30 dBZ). The control experiment, Exp. Control, which does not use the GSWR product, shows low FSS at all reflectivity thresholds, with values ≤0.1 at the 10-dBZ threshold (Fig. 12a) but reaching lower peaks at the higher thresholds (Fig. 13a, and Fig. 14a). The assimilation of GSWR data improves the FSS, with Exp. GSWR having values around 0.5 (Fig. 12b, Fig. 13b, and Fig. 14b), and somewhat higher at the 30-dBZ threshold. Allowing RDLH to trigger the decreasing of precipitation hydrometeors (Exp. GSWR_H) increases FSS in the first hour from approximately 0.50 to approximately 0.65 for the 10-dBZ threshold (Fig. 12c), from approximately 0.53 to approximately 0.58 for the 20-dBZ threshold (Fig. 13c), and seems to make little difference at 30 dBZ (Fig. 14c). Adding 1) observations to the initial condition analysis and 2) observation nudging during the pre-forecast appears to have little impact on FSS (Exp. GSWR_HN in Fig. 12d, Fig. 13d, and Fig. 14d). For this case, the implementation in Exp. GSWR_HL of the RDLH limiter (to lessen shocks from high RDLH being imposed where the model previously had much less microphysics related heating [MPHT]), resulted in a notable decrease in FSS at 10 dBZ (Fig. 12e) and 20 dBZ (Fig. 13e) compared to Exp. GSWR_H, but little change at 30 dBZ (Fig. 14e). It may be that although the limiter helps to avoid shocks, as a side effect, it does not assimilate the GSWR data as well. Allowing RDLH to be used to trigger a decrease in the water vapor mixing ratio notably increases FSS at 10 dBZ (Fig. 12f) and 20 dBZ (Fig. 13f) to the highest level of any experiment during the first forecast hour but results in little change in FSS at 30 dBZ (Fig. 14f).

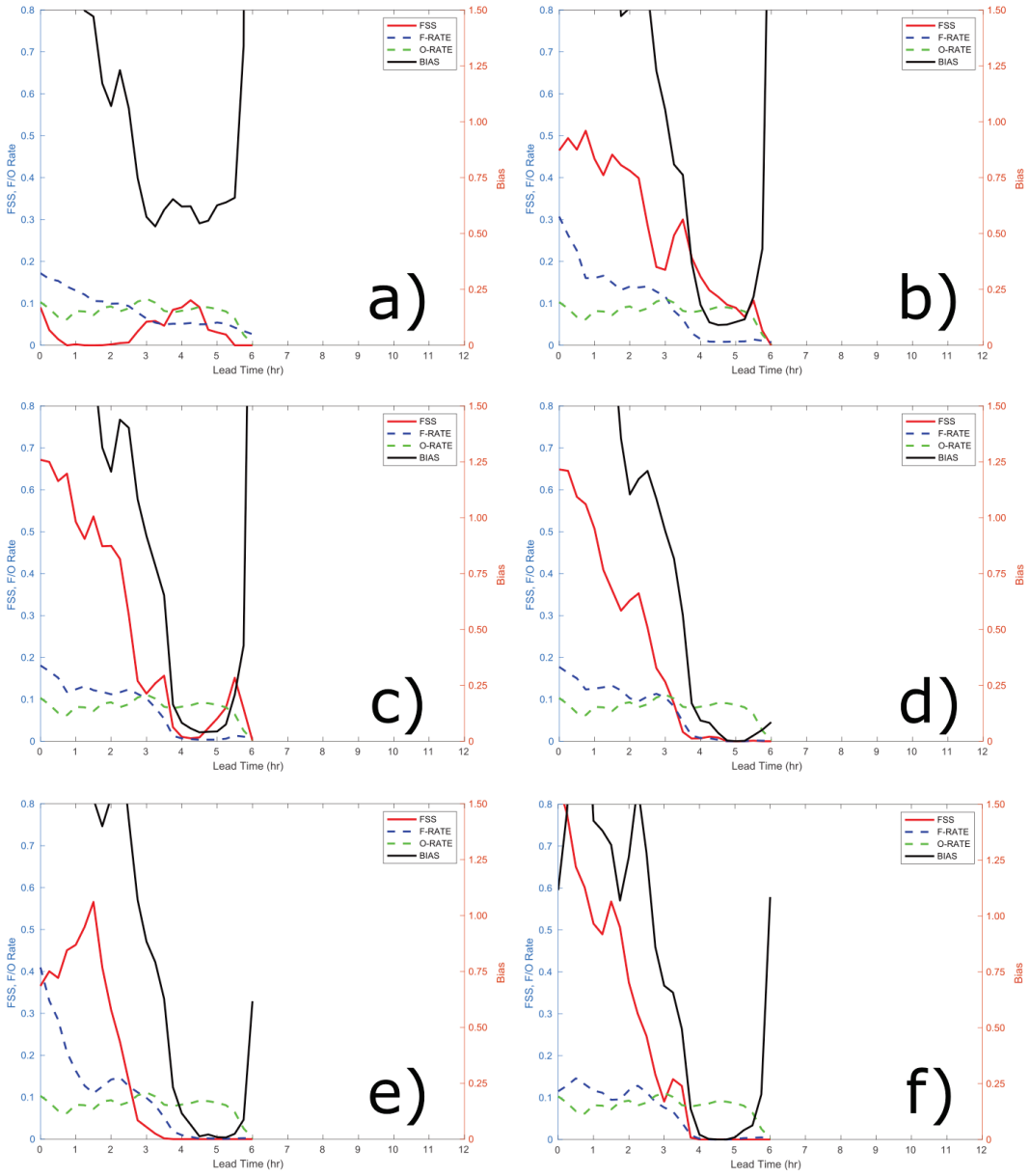

Fig. 12 Time series comparing WRF_{CMR} from the 1-km domain to $GSWR_{CMR}$ using a 10-dBZ threshold for 11-km neighborhood FSS, bias, as well as the observed rate (O-RATE) and forecast rate (F-RATE) used to calculate bias. Results are shown for the Black Sea simulations for experiments a) Control, b) GSWR, c) GSWR_H, d) GSWR_HN, e) GSWR_HL, and f) GSWR_HLV.

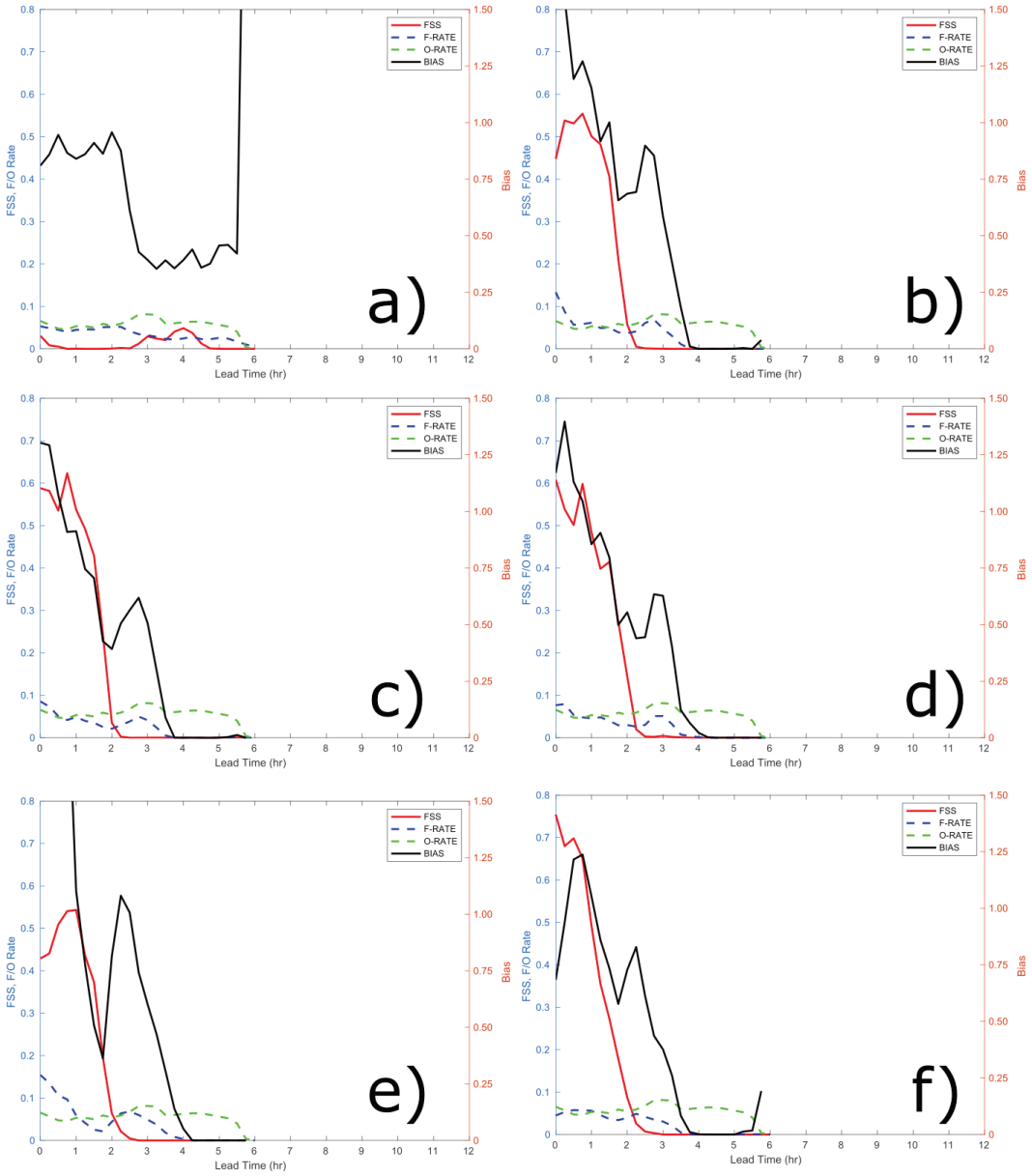

Fig. 13 Time series comparing WRF_{CMR} from the 1-km domain to $GSWR_{CMR}$ using a 20-dBZ threshold for 11-km neighborhood FSS, bias, as well as the O-RATE and F-RATE used to calculate bias. Results are shown for the Black Sea simulations for experiments a) Control, b) GSWR, c) GSWR_H, d) GSWR_HN, e) GSWR_HL, and f) GSWR_HLV.

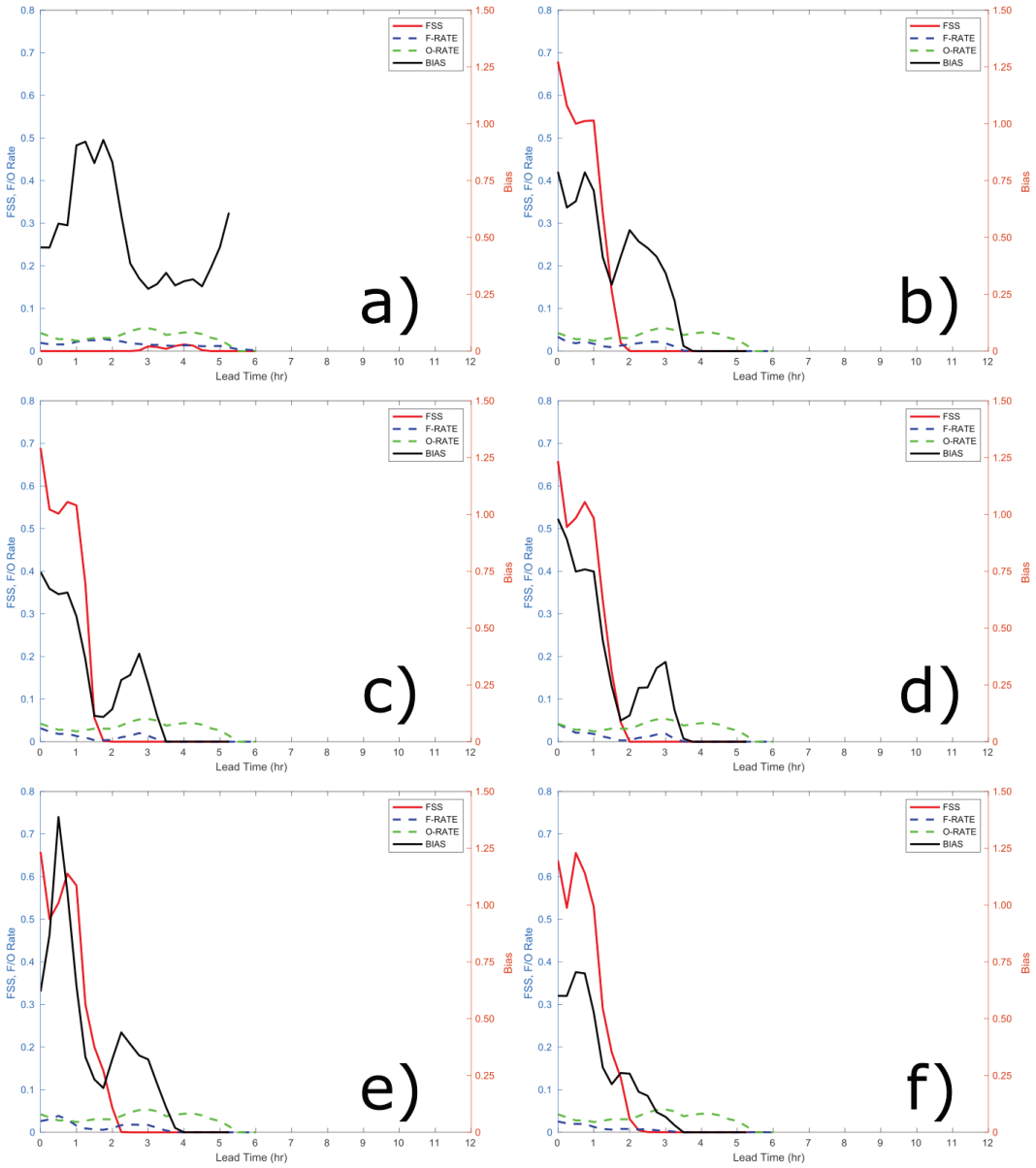

Fig. 14 Time series comparing WRF_{CMR} from the 1-km domain to $GSWR_{CMR}$ using a 30-dBZ threshold for 11-km neighborhood FSS, bias, as well as the O-RATE and F-RATE used to calculate bias. Results are shown for the Black Sea simulations for experiments a) Control, b) GSWR, c) GSWR_H, d) GSWR_HN, e) GSWR_HL, and f) GSWR_HLV.

In terms of bias for the Black Sea experiments, at 10 dBZ (Fig. 12) all experiments have an overforecast bias at the beginning of the forecast that turns into an underforecast bias during the forecast period, and then at the end of the forecast period the bias starts increasing (whether it becomes an overforecast bias or not depends on the experiment). All of the experiments that assimilate GSWR data worsen the underforecast at 10 dBZ in the 4.0- to 5.5-h forecast period. At 20 dBZ the control experiment (Fig. 13a) has a slight underforecast bias in the 0- to 2-h period, followed by a more substantial underforecast bias in the 3- to 5-h period, and then an overforecast bias at the very end of the period. The experiments assimilating GSWR (Fig. 13b–f) all worsen the underforecast bias in the 4.0- to 5.5-h period at the 20-dBZ threshold, as is also the case at 10 dBZ. At 30 dBZ (Fig. 14) the experiments assimilating GSWR improved the bias in the 0- to 1-h period but appeared to increase the underforecast bias during the rest of the experiment. The experiments assimilating GSWR missed much of the convection in the 4.0- to 5.5-h period leading to generally near-zero biases and FSS.

7.2 Far Western Russia Case

Figure 15 compares WRF_{CMR} for each of the experiments on the 1-km domain at the 0-h forecast time (1300 UTC) with the $GSWR_{CMR}$ valid at that time. The $GSWR_{CMR}$ field (Fig. 15g) indicates the main feature is an area of reflectivities reaching 30 dBZ in the southwest corner of the domain. The experiment without GSWR assimilation (Exp. Control, Fig. 15a) also shows an area of enhanced reflectivity in the southwest corner, but contrary to $GSWR_{CMR}$ shows widespread reflectivity throughout the domain. Adding GSWR assimilation (Exp. GSWR, Fig. 15b) results in the feature in the southwest corner more closely matching $GSWR_{CMR}$, and the reflectivity across the rest of the domain is substantially decreased. Allowing $GSWR_{CMR}$ to directly modify hydrometeors (Exp. GSWR_H, Fig. 15c) decreases the apparently erroneous reflectivities outside the southwest corner. Adding assimilation of other observations (Exp. GSWR_HN, Fig. 15d) and the RDLH limiter (Exp. GSWR_HL, Fig. 15e) has minimal effects. However, allowing the $GSWR_{CMR}$ to affect water vapor directly (Exp. GSWR_HLV, Fig. 15f) results in much of the apparently erroneous reflectivity being removed.

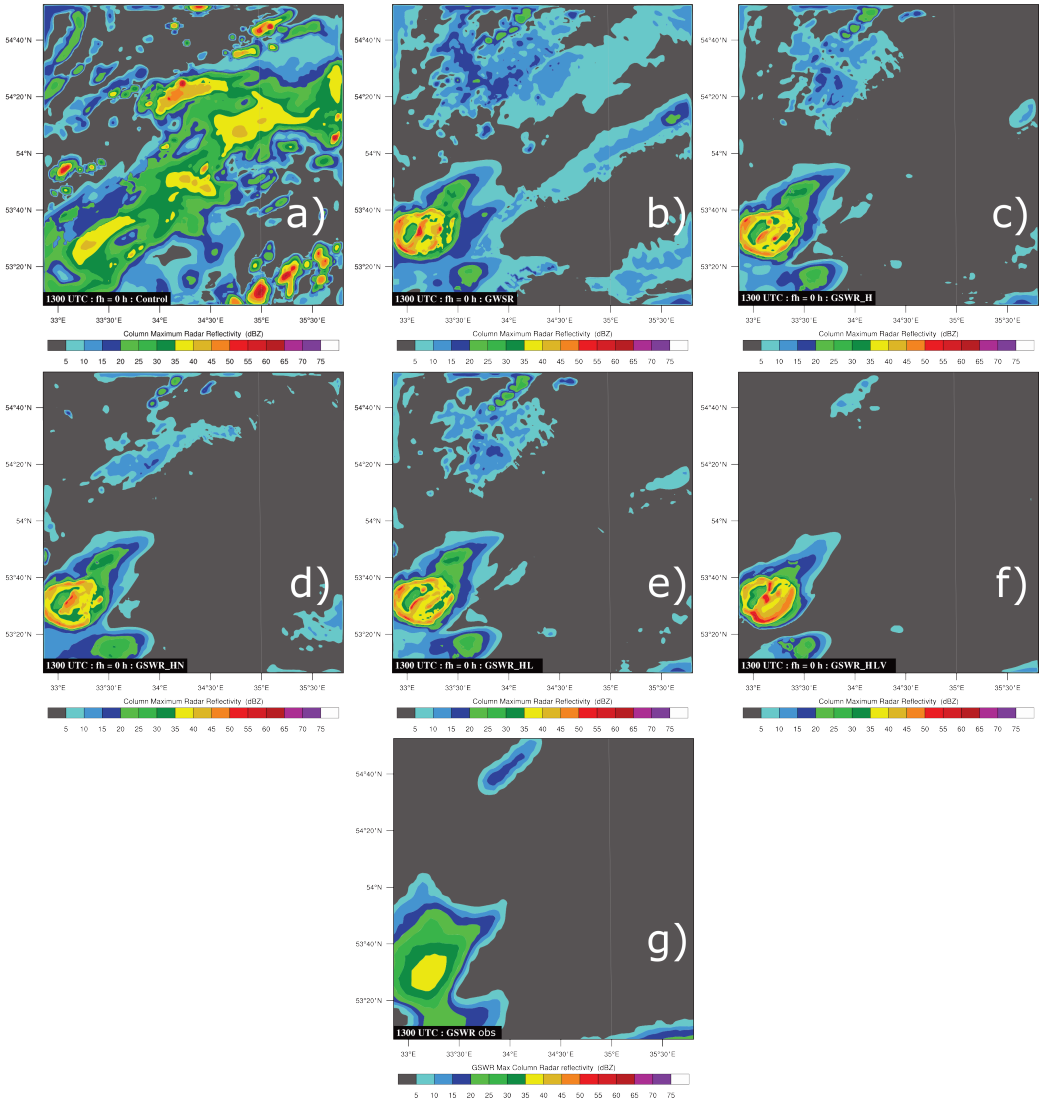

Fig. 15 WRF_{CMR} for the far western Russia case for Exps. a) Control, b) GSWR, c) GSWR_H, d) GSWR_HN, e) GSWR_HL, f) GSWR_HLV at the 0-h forecast time (1300 UTC), and g) $GSWR_{CMR}$ for 1300 UTC. In the lower-left-hand corner of the black box of each WRF_{CMR} plot (a–f), the text "fh = 0 h" indicates that the 0-h forecast is plotted.

For the far western Russia experiments, verification plots for the 1-km domain at 10-, 20-, and 30-dBZ thresholds are shown in Figs. 16, 17, and 18, respectively. At the 10-dBZ threshold (Fig. 16) all experiments assimilating GSWR perform better than the control experiment in terms of FSS during the first forecast hour, but worse than the control experiment around the 2-h forecast. Most of the GSWR experiments also outperform the control experiment in terms of FSS around the 4-h forecast. Among the GSWR experiments, during the first hour Exp. GSWR performs somewhat worse than the other GSWR experiments, while the other GSWR experiments perform similarly (although Exp. GSWR_HLV has a slightly lower FSS in the first 15 min). Consistent with the 10-dBZ threshold, at the 20-dBZ (Fig. 17) and 30-dBZ (Fig. 18) thresholds, all of the GSWR experiments outperform the control experiment in terms of FSS over the first hour, but perform more poorly at the 2-h forecast. Among the GSWR experiments it is difficult to see notable differences in FSS for these thresholds. In terms of bias, the control experiment had a significant overforecasting bias at the 0-h forecast for all three thresholds, which was notably improved in all of the GSWR experiments at all three thresholds. Among the GSWR experiments, at 10 dBZ for bias at 0-h Exp. GSWR performs the worst, GSWR_HLV is the next best, and Exps. GSWR_H, GSWR_HN, and GSWR_HL perform very similarly with biases very close to 1.0. At 20 and 30 dBZ the 0-h bias indicates that most of the GSWR experiments perform very similarly, with GSWR_HLV slightly worse. After the 0-h forecast time, all experiments at all thresholds shift to an underforecast bias and then eventually to an overforecast bias. Since the observations do not indicate any reflectivities (at least any >10 dBZ) in the 5- to 6-h forecast period but the model does forecast such reflectivities, the FSS is 0.0 and the bias is undefined.

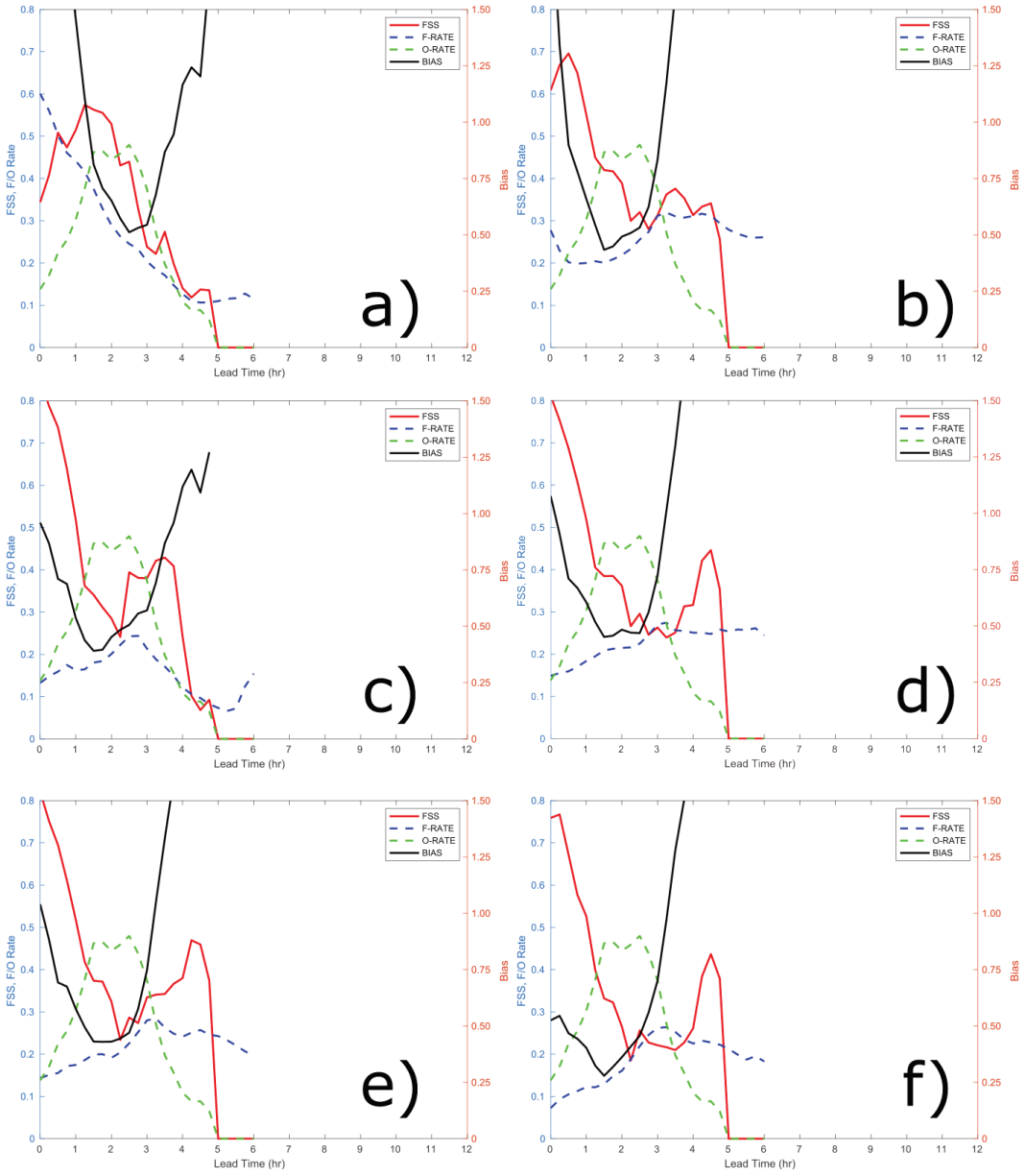

Fig. 16 Time series comparing WRF_{CMR} from the 1-km domain to $GSWR_{CMR}$ using a 10-dBZ threshold for 11-km neighborhood FSS, bias, as well as the O-RATE and F-RATE used to calculate bias. Results are shown for the far western Russia simulations for Exps. a) Control, b) GSWR, c) GSWR_H, d) GSWR_HN, f) GSWR_HL, and e) GSWR_HLV.

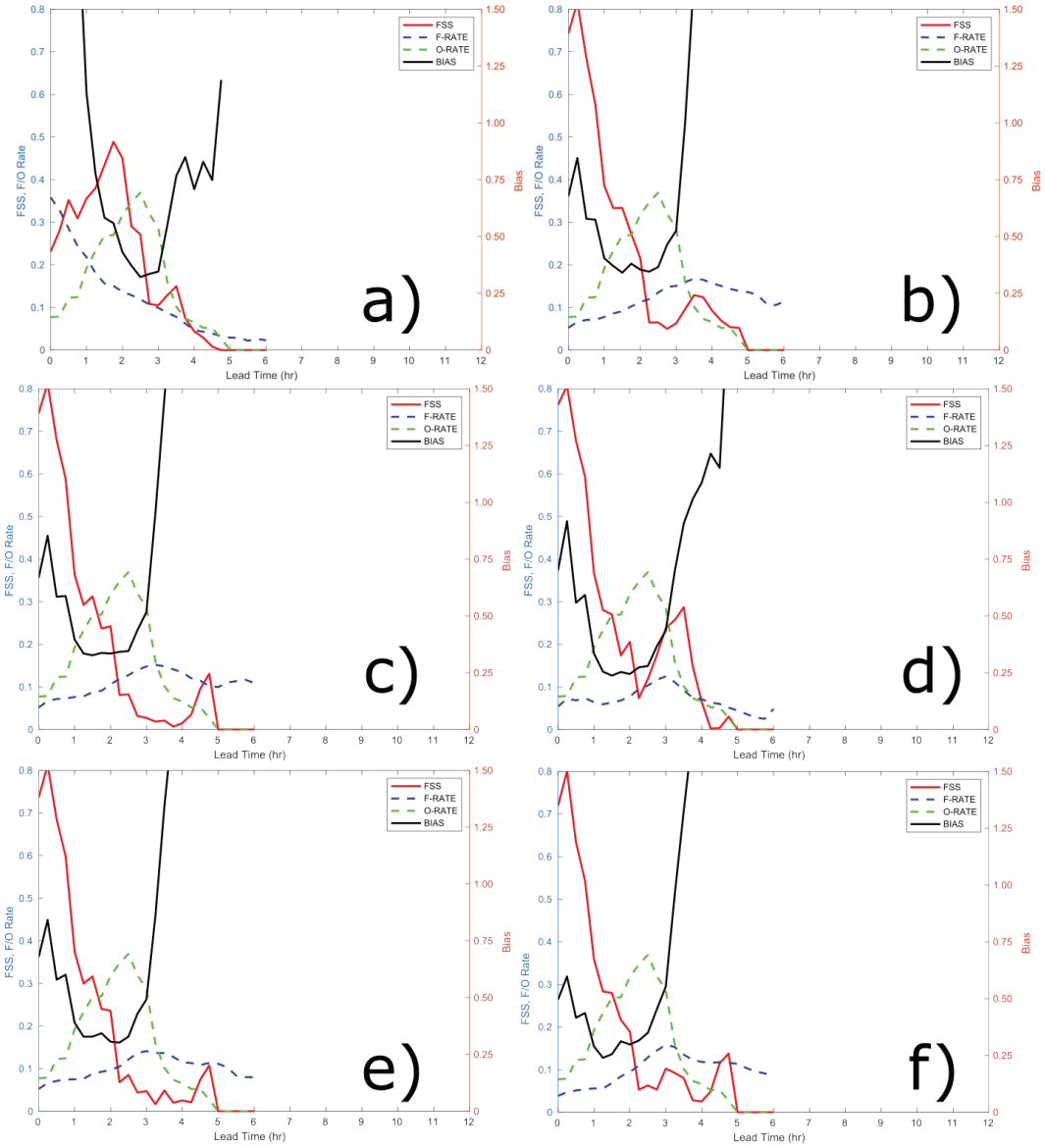

Fig. 17 Time series comparing WRF_{CMR} from the 1-km domain to $GSWR_{CMR}$ using a 20-dBZ threshold for 11-km neighborhood FSS, bias, as well as the O-RATE and F-RATE used to calculate bias. Results are shown for the far western Russia simulations for Exps. a) Control, b) GSWR, c) GSWR_H, d) GSWR_HN, f) GSWR_HL, and e) GSWR_HLV.

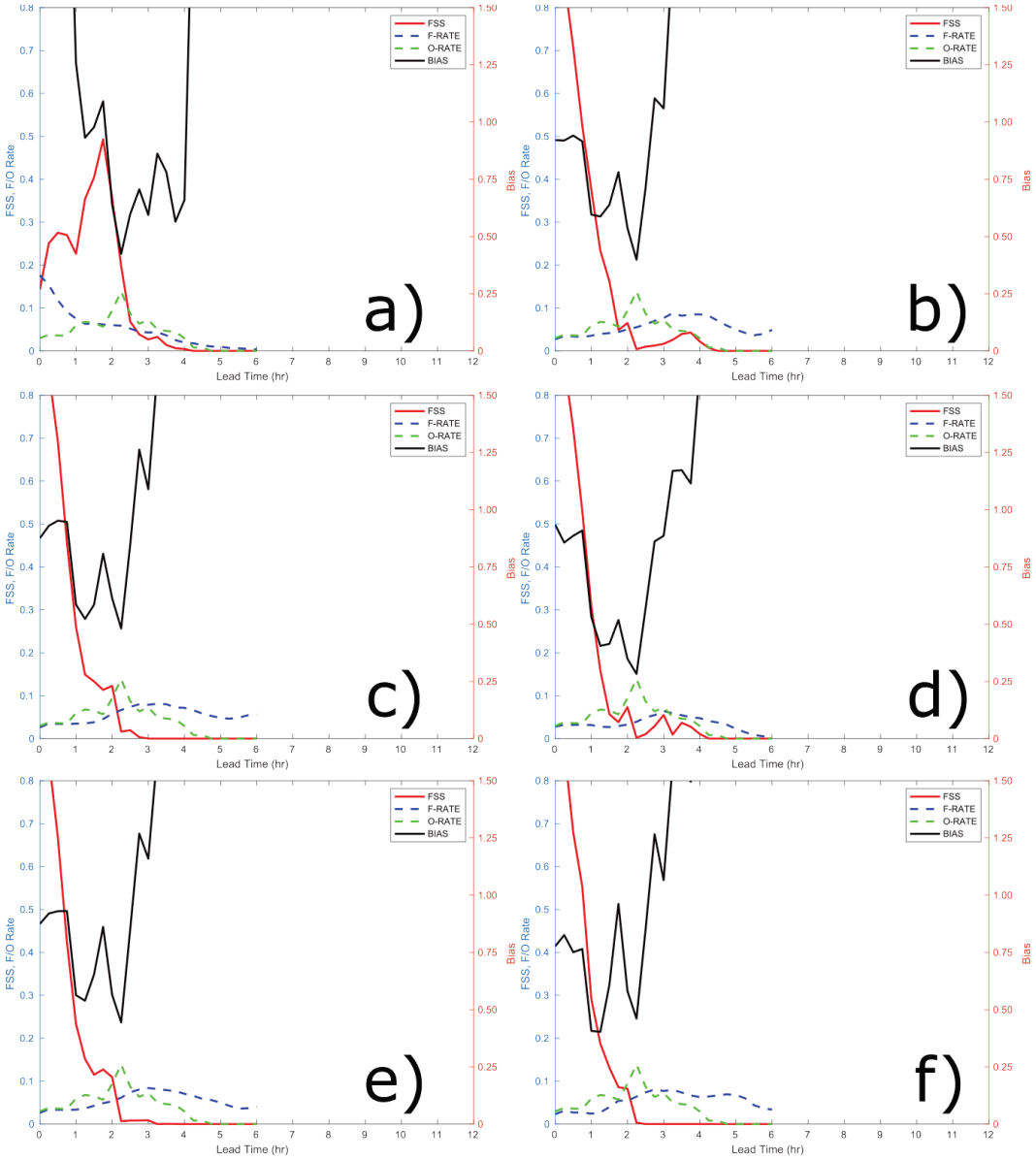

Fig. 18 Time series comparing WRF_{CMR} from the 1-km domain to $GSWR_{CMR}$ using a 30-dBZ threshold for 11-km neighborhood FSS, bias, as well as the O-RATE and F-RATE used to calculate bias. Results are shown for the far western Russia simulations for Exps. a) Control, b) GSWR, c) GSWR_H, d) GSWR_HN, e) GSWR_HL, and f) GSWR_HLV.

8. Conclusion and Future Work

The method used to assimilate 3-D radar reflectivity data in Reen et al. (2019) was applied to assimilate column maximum reflectivity from GSWR ($GSWR_{CMR}$) for two domains on the same day. In order to do this a methodology was developed to estimate a vertical profile of reflectivity from $GSWR_{CMR}$ so that a 3-D RDLH could be calculated. The methodology leverages the WRF reflectivity profile when it is sufficiently strong and falls back to using reference reflectivity profiles when the WRF reflectivity profile is weak relative to GSWR. Experiments were carried out to test the impact of assimilating the GSWR data and evaluate modifications to the assimilation technique.

The results of the experiments indicate that GSWR can improve the FSS in the short-term forecast and that modifications to the assimilation technique improve the forecast results further. Overall, Exp. GSWR_HLV may have performed best. This experiment allowed GSWR to be used to decrease precipitation hydrometeors, cloud water, and water vapor where GSWR indicates that WRF is incorrectly forecasting moist convection. This experiment also included a limiter to ameliorate issues seen where assimilation of high reflectivities could cause apparently unrealistic features in the simulation. This study examined only two cases and so examination of additional cases would more fully evaluate the value of GSWR and allow for improvement of the assimilation technique.

In this study, the GSWR data were assumed to be "truth" as actual radar data were not available for verification. Work is underway to assimilate GSWR data in a region where radar data are available so that the accuracy of the WRF forecast can be evaluated against the radar data and the accuracy of the GSWR data can be evaluated. GSWR is produced by merging information from multiple datasets together based on relationships between datasets observed in the past and thus will likely have more error than more direct observations such as radar. The spatial resolution of the input data used to create GSWR is likely coarser than radar data and consistent with this, the GSWR output data are provided at a grid spacing (5 km) coarser than the radar data. Additionally, since GSWR does not provide a vertical profile, the process of converting a single value into a vertical profile will introduce error. Thus, the information provided by GSWR is expected to be inferior to that which would be provided by weather radar.

The results of this study suggest that GSWR data are valuable for improving short-term forecasts. GSWR appears to be a promising data source for assimilating in the vast regions of the earth where weather radar is unavailable. However, given the superiority expected to exist in the information provided from radar as compared

to that provided from GSWR, it is strongly recommended that if both radar and GSWR data are available that radar data should be assimilated.

9. References

Alexander C, Dowell D, Hu M, Ladwig T, Weygandt S, Benjamin SG. Expanding use of radar data in deterministic and ensemble data assimilation for the High-Resolution Rapid Refresh (HRRR). Presented at 38th Conference on Radar Meteorology; American Meteorological Society; 2017 Aug 28–Sep 1; Chicago, IL. 19B.2. c2017 [accessed 2020 Aug 18]. https://ams.confex.com/ams/38RADAR/webprogram/Paper321169.html.

Benjamin SG, Weygandt S, Brown JM, Hu M, Alexander CR, Smirnova TG, Olson JB, James EP, Dowell DC, Grell GA, et al. A North American hourly assimilation and model forecast cycle: the Rapid Refresh. Mon Weather Rev. 2016;144(4):669–1694.

Grell GA. Freitas SR. A scale and aerosol aware stochastic convective parameterization for weather and air quality modeling. Atmos Chem Phys. 2014;14:5233–5250. doi:10.5194/acp-14-5233-2014.

Iacono MJ, Delamere JS, Mlawer EJ, Shephard MW, Clough SA, Collins WD. Radiative forcing by long-lived greenhouse gases: calculations with the AER radiative transfer models. J Geophys Res. 2008;113:D13103. doi:10.1029/ 2008JD009944.

Nakanishi M, Niino H. An improved Mellor–Yamada level 3 model: its numerical stability and application to a regional prediction of advecting fog. Boundary Layer Met. 2006;119:397–407. doi:10.1007/s10546-005-9030-8.

Nakanishi M, Niino H. Development of an improved turbulence closure model for the atmospheric boundary layer. J Meteor Soc Japan. 2009;87:895–912. doi:10.2151/jmsj.87.895.

[NCAR] National Center for Atmospheric Research. User's guide for the Advanced Research WRF (ARW) modeling system version 4.1. Boulder (CO): National Center for Atmospheric Research; 2019 [accessed 2020 August 14]. https://www2.mmm.ucar.edu/wrf/users/docs/user_guide_v4/v4.1/contents.html.

Olson JB, Kenyon JS, Angevine WM, Brown JM, Pagowski M, Sušelj K. A description of the MYNN-EDMF scheme and the coupling to other components in WRF–ARW. Boulder (CO): National Oceanic and Atmospheric Administration Earth System Research Laboratory Global Systems Division; 2019. NOAA Technical Memorandum OAR GSD 61. doi:10.25923/n9wm-be49.

Reen BP, Cai H, Raby JW. Radar assimilation over Kwajalein Atoll. Adelphi (MD): US Army Combat Capabilities Development Command, Army Research Laboratory; 2019 Oct. Report No.: ARL-TR-8831. https://apps.dtic.mil/sti/pdfs/AD1082516.pdf.

Reen BP, Dawson LP. The Weather Running Estimate–Nowcast Realtime (WREN_RT) system, version 1.03. Adelphi Laboratory Center (MD): Army Research Laboratory (US); 2018 Sep. Report No.: ARL-TR-8533. https://apps.dtic.mil/sti/pdfs/AD1060869.pdf.

Roberts N, Lean H. Scale-selective verification of rainfall accumulations from high-resolution forecasts of convective events. Mon Wea Rev. 2008;136:78–97.

Roberts N. Assessing the spatial and temporal variation in the skill of precipitation forecasts from an NWP model. Meteor Appl. 2008;15:163–169.

Shao H, Derber J, Huang X-Y, Hu M, Newman K, Stark D, Lueken M, Zhou C, Nance L, Kuo Y-H, Brown B. Bridging research to operations transitions: status and plans of community GSI. B Am Meteorol Soc. 2016;97:1427–1440. doi: 10.1175/BAMS-D-13-00245.1.

Skamarock WC, Klemp JB, Dudhia J, Gill DO, Barker DM, Duda M, Huang XY, Wang W, Powers JG. A description of the Advanced Research WRF version 3. Boulder (CO): National Center for Atmospheric Research; 2008. Report No.: 475. http://www2.mmm.ucar.edu/wrf/users/docs/arw_v3_bw.pdf.

Skamarock WC, Klemp JB, Dudhia J, Gill DO, Liu Z, Berner J, Wang W, Powers JG, Duda MG, Barker DM, Huang, X-Y. A description of the advanced research WRF model version 4. Boulder (CO): National Center for Atmospheric Research; 2019 Report No. NCAR/TN-556+STR. doi:10.5065/1dfh-6p97.

Tewari M, Chen F, Wang W, Dudhia J, LeMone MA, Mitchell K, Ek M, Gayno G, Wegiel J, Cuenca RH. Implementation and verification of the unified NOAH land surface model in the WRF model. In: 20th Conference on Weather Analysis and Forecasting/16th Conference on Numerical Weather Prediction; 2004 Jan 12–16; Seattle, WA. Seattle (WA): American Meteorological Society. c2004. p. 11–15.

Thompson G, Eidhammer T. A study of aerosol impacts on clouds and precipitation development in a large winter cyclone. J Atmos Sci. 2014;71.10:3636–3658. doi:10.1175/JAS-D-13-0305.1

Veillette MS, Hassey EP, Mattioli CJ, Iskenderian H, Lamey PM. Creating synthetic radar imagery using convolutional neural networks. J Atmos Oceanic Technol. 2018:35(12):2328-2338. doi:10.1175/JTECH-D-18-0010.1.

Veillette MS, Iskenderian H, Lamey PM, Mattioli CJ, Banerjee A, Worris M, Porschitsky AB, Ferris RF, Manwelyan A, Rajagoplalan S, Usmani H, Coe TE, Luce JE, Esgar BA. Global synthetic weather radar in AWS GovCloud for the U.S. Air Force. Presented at 19th Conference on Artificial Intelligence for Environmental Science; American Meteorological Society; 2020 Jan 13–16; Boston, MA. J69.3. https://ams.confex.com/ams/2020Annual/meetingapp.cgi/Paper/363150.

List of Symbols, Abbreviations, and Acronyms

3-D	three-dimensional
ARL	Army Research Laboratory
CCDC	US Army Combat Capabilities Development Command
CMR	column maximum reflectivity
CONUS	continental United States
CPHT	cumulus parameterization heating term
F-RATE	forecast rate
FSS	fractions skill score
GFS	Global Forecast System
GOES	Geostationary Operational Environment Satellite
GSI	Gridpoint Statistical Interpolation
GSWR	Global Synthetic Weather Radar
HRRR	High-Resolution Rapid Refresh
MADIS	Meteorological Assimilation Data Ingest System
MET	Model Evaluation Tools
METAR	Météorologique Aviation Régulière
MIT-LL	Massachusetts Institute of Technology – Lincoln Laboratory
MPHT	microphysics heating term
MYNN	Mellor–Yamada Nakanishi Niino scheme
NCAR	National Center for Atmospheric Research
NWP	numerical weather prediction
O-RATE	observed rate
RDLH	reflectivity-derived latent heating
RRTMG	rapid radiative transfer model for general circulation
UTC	coordinated universal time
WREN_RT	Weather Running Estimate–Nowcast Realtime system

WRF	Weather Research and Forecasting model
WRF-ARW	Advanced Research version of the Weather Research and Forecasting model

1 (PDF)	DEFENSE TECHNICAL INFORMATION CTR DTIC OCA
1 (PDF)	CCDC ARL FCDD RLD DCI TECH LIB
3 (PDF)	CCDC ARL FCDD RLC EM B REEN H CAI J RABY